

A Study of Strangeness Production and Decay Processes using a Very Forward Particle Trigger in Photo- and Electroproduction

Leter of Intent

May 24, 2004

Henry Juengst, William Briscoe
George Washington University
Washington, DC
(757)269-6673
juengst@moose.jlab.org

—
Ed V. Hungerford, K. J. Lan, T. Miyoshi, Graduate Students,
University of Houston
Houston, TX 77204
(713)743-3549
hunger@uh.edu

—
Liguang Tang
Hampton University
Hampton, VA
(757)269-
ltang@jlab.org

—
Local Contact
Henry Juengst
(757)269-6673
juengst@moose.jlab.org

1 Summary

We propose to study the production of various strange particles and strange nuclear systems using photo- and electro-production at zero degrees in combination with a very forward angle particle trigger. The new feature of this LOI is that a kaon trigger is implemented for kaons produced at angles ≤ 15 degrees. In addition, for electroproduction processes the scattered electrons are also detected at essentially zero degrees with respect to the incident beam.

As an example on the physics to be studied, we would propose to investigate the dynamical behavior of the $\Delta I = 1/2$ rule by measuring nucleon emission in the non-mesonic decay of the ${}^4_{\Lambda}\text{H}$ hypernucleus. For this experiment, energy resolution sufficient to identify the production of a hypernucleus is necessary (≈ 10 MeV FWHM). The hypernuclear decay products are detected in CLAS.

The experiment uses photons, either real or virtual, incident on a liquid ${}^4\text{He}$ target to produce the ${}^4_{\Lambda}\text{H}$ hypernucleus via the (γ, K^+) reaction. The goal of the experiment is to combine the measured strength of the neutron and proton stimulated decays from this hypernucleus with similar values from other s-shell hypernuclei, in order to obtain a definitive test of the $\Delta I=1/2$ rule in a high momentum-transfer, weak decay. We intend to obtain both coincident and singles spectra of the neutron and proton stimulated decay.

We expect to obtain neutron-proton and neutron-neutron coincident events, as well as the singles spectra. The experiment will provide the first definitive test of the $\Delta I = 1/2$ rule in a non-mesonic decay process.

2 Background

2.1 Hyperon Weak Decay and the $\Delta I = 1/2$ Rule

A free Λ decays principally via the pionic modes [1];

$$\begin{aligned}\Lambda &\rightarrow p + \pi^- + 38 \text{ MeV} && (64\%) \\ &\rightarrow n + \pi^0 + 41 \text{ MeV}; && (36\%) \end{aligned}$$

with a lifetime of;

$$\tau = \hbar/\Gamma_\Lambda = 2.63 \times 10^{-10} \text{ s}.$$

In this equation, Γ_Λ is the total decay width, and in terms of pionic partial decay widths, it is written;

$$\Gamma_\Lambda = \Gamma_{\pi^-} + \Gamma_{\pi^0}.$$

The decay changes strangeness by $\Delta S=1$, and this can occur with an isospin change of $\Delta I=1/2$ or $3/2$. Indeed a weak ($V - A$) Hamiltonian description of the transition provides comparable $\Delta I=1/2$ and $3/2$ strengths. Experimentally however, the $\Delta I=1/2$ amplitudes for mesonic $\Delta S = 1$ decays for hyperons [?] and kaons [?] are found to be enhanced by roughly a factor of 20 relative to the $\Delta I=3/2$ amplitudes. As an example, for Λ decay one finds:

$$\Gamma_{\pi^-}/\Gamma_{\pi^0} \cong 1.9 .$$

This value is approximately the ratio of the square of the isospin Clebsch-Gordan coefficients for a pure $\Delta I=1/2$ weak decay operator, and implies a large enhancement of the $\Delta I=1/2$ amplitude. The result of these strangeness-changing mesonic decays of hyperons and kaons is then generalized into the empirical “ $\Delta I=1/2$ rule”, which states that the non-leptonic decays of all strange hadrons proceeds predominately through $\Delta I = 1/2$ amplitudes (see for example, reference [2]).

There is no universal explanation for this apparently universal rule. It is accepted that a modest enhancement comes from leading-log QCD corrections associated with “hard-gluon” exchanges [3]. The remainder has been explained only in a case-by-case basis. For example, in kaon decays $K \rightarrow \pi\pi$ the strong attraction in the $I = 0$ final state channel is thought to be responsible for the effect [5], but such final-state interactions do not explain the hyperon results. Okun [4] argues that the enhancement seen in hyperon decays is a result of the pseudoscalar nature of the pion and its association with the dominant internal diagrams. It is also known that penguin graphs produce non-trivial contributions [3]. Given that there is not a common mechanism to explain the $\Delta I = 1/2$ rule, it is likely that it involves complicated dynamics of the decay of the strange quark. However, we note that the rule has only been tested in the low-momentum, long-range pionic decays of strange hyperons and mesons. As will be discussed in somewhat more detail later, theoretical treatments of

higher momentum transfer processes involving non-mesonic weak decays, predict strong violations of this rule.

2.2 Weak Decay of Λ Hypernuclei

The energy release in mesonic Λ decay, and the mass difference between the nucleon and pion means that the nucleon receives only some 100 MeV/c of momentum in the decay process. If the Λ resides in the ground state of a hypernucleus, the recoiling nucleon has momentum below the Fermi momentum-surface (about 280 MeV/c), and thus pionic decay of hypernuclei, particularly heavy hypernuclei, is Pauli suppressed.

Indeed of interest to a future proposal is the fact that pionic decay of heavier hypernuclei is only suppressed [7] by a factor of $\cong 100$. This is due to correlations and high momentum components in the single-particle wave functions. In addition, the unfilled nuclear states have a dramatic effect on the ratio of π^-/π^0 decays. For example in the mesonic decay of the s-shell hypernucleus, ${}^4_\Lambda\text{He}$, the ratio, $\Gamma({}^4_\Lambda\text{He} \rightarrow \pi^0)/\Gamma({}^4_\Lambda\text{He} \rightarrow \pi^-)$, is sensitive to the nuclear wave functions because in the π^- decay of ${}^4_\Lambda\text{He}$, the proton 1s-shell is already filled.

Also one finds that [11]:

$$\frac{\Gamma({}^4_\Lambda\text{He} \rightarrow \pi^+ + (\text{pnnn}))}{\Gamma({}^4_\Lambda\text{He} \rightarrow \pi^- + (\text{pppn}))} \approx 0.043 \pm 0.017;$$

Note that the presence of a π^+ in the final state means the process must occur through some intermediate step, e.g. $\Lambda - \Sigma$ mixing or pionic charge exchange, as a π^+ does not occur in free Λ decay. Given the present ability to generate few-body wave functions with realistic NN and YN interactions, one could make significant tests of the nuclear properties by comparing experimentally observed decay rates to various nuclear models.

However the LOI discussed here focuses on non-mesonic decay, which can only occur within the nuclear medium[8],.

$$\begin{aligned} \Lambda n &\rightarrow nn + 176 \text{ MeV}; \text{ or} \\ \Lambda p &\rightarrow np + 176 \text{ MeV}. \end{aligned}$$

The kinematics of these decays provides a momentum of about 400 MeV/c to each final-state nucleon, which is well above the Fermi momentum[19]. Because mesonic decay is suppressed by Pauli blocking of the recoil nucleons, non-mesonic decay dominates in all but the lightest hypernuclei, and the large momentum transfer means that sub-nucleon degrees of freedom are probably important. One also notes that non-mesonic decay is the only practical method to study the four-fermion, weak-decay vertex. Thus within a nucleus, the total decay width can be written as a sum of the various partial widths.

$$\Gamma_\Lambda = \Gamma_{\pi^-} + \Gamma_{\pi^0} + \Gamma_{nn} + \Gamma_{np}.$$

In principle, the total and each partial decay width can be independently measured. In practice because of experimental difficulties, Γ_{π^0} is usually inferred by measuring the other four quantities [12]. The total non-mesonic width, $\Gamma_{nm} = \Gamma_{np} + \Gamma_{nn}$, seems relatively insensitive to the details of a weak interaction model, but certainly depends as indicated above, on the nuclear physics. However the ratio, Γ_{nn}/Γ_{np} is strongly dependent on the weak interaction model. In particular it is not clear if the $\Delta I = 1/2$ rule applies in non-mesonic decay, and in fact there is some experimental evidence that it does not [21]. Furthermore, if the non-mesonic decay is treated theoretically by a meson exchange interaction, the Γ_{nn}/Γ_{np} ratio is sensitive to specific mesonic exchange components, i.e. π , ρ , K, etc., and of course to the imposition of the $\Delta I = 1/2$ rule.

The non-mesonic weak decay process does not conserve parity, isospin, or strangeness. Parity violation (PV) can be used to tag the weak NN interaction, and as a consequence only the PV components of the interaction are probed. In contrast, strangeness violation can be used to tag

Table 1: Allowed Transitions in $(2I+1)(2S+1)L_J$ Notation

$\Lambda N \rightarrow NN$	I_{NN}	S_{NN}
$^{31}S_0 \rightarrow ^{31}S_0$	1	0
$^{31}S_0 \rightarrow ^{33}P_0$	1	1
$^{13}S_1 \rightarrow ^{33}P_1$	1	1
$^{13}S_1 \rightarrow ^{13}S_1$	0	1
$^{13}S_1 \rightarrow ^{13}D_1$	0	1
$^{13}S_1 \rightarrow ^{11}P_1$	0	0

the weak $\Lambda N \rightarrow NN$ transition, and thus both the parity-conserving (PC) and PV components are probed[19, 20]. Of particular interest is the polarization asymmetry of the non-mesonic decay, which can be defined by the angular distribution of the protons in the non-mesonic decay of a polarized hypernucleus. The asymmetry between the number of protons emitted along and opposite to the polarization direction is due to the interference between the parity-violating and parity conserving amplitudes with different values of NN isospin. Thus due to the asymmetry of the NN state, the $\Lambda N \rightarrow NN$ parity-violating and parity-conserving amplitudes correspond to S(spin) + I(isospin) even and S + I odd, respectively, and the interference terms in the proton asymmetry occur between the same intrinsic S states. The non-mesonic partial rates are dominated by the parity-conserving amplitudes. The asymmetry of the outgoing protons has the form;

$$A(\theta, J) = p_\Lambda(J) a_\Lambda \cos(\theta).$$

In this expression, p_Λ is the polarization of the Λ which can be related to that of the hypernucleus once the nuclear structure is known, and a_Λ is the non-mesonic decay asymmetry factor. Therefore both the partial decay rates and decay asymmetry can provide information on the ΛN interaction within the nuclear medium.

If the ΛN interaction occurs in a relative s-state, there are six allowed amplitudes, as listed in Table 1, but for example, only the $I_{nn}=1$ final states are available to neutron-stimulated ΛN decay. Thus the respective decay rates are given by:

$$\begin{aligned} \Gamma_{nn} &= 2[\Gamma(^{31}S_0) + \Gamma(^{33}P_0) + \Gamma(^{33}P_1)]; \\ \Gamma_{np} &= [\Gamma(^{31}S_0) + \Gamma(^{33}P_0) + \Gamma(^{33}P_1) + \Gamma(^{13}S_1) + \Gamma(^{13}D_1) + \Gamma(^{11}P_1)]. \end{aligned}$$

The factor of 2 on the right-hand side of the expression for Γ_{nn} is due to the assumed $\Delta I = 1/2$ rule. The $^{13}S_1 \rightarrow ^{13}D_1$ tensor transition, which is only open to the proton channel, is expected to dominate the long range pion exchange component of the interaction. Simple calculations based only on π and ρ exchange exhibit a dominance of transitions from the $^{13}S_1$ state over the $^{31}S_0$ transitions, owing primarily to the tensor transition. Consequently, nearly all models predict the $\Lambda n \rightarrow nn$ widths of hypernuclei to be vanishingly small (see, for example ref. [16], and references therein). Experimentally one finds;

$$0.6 \leq \Gamma_{nn}/\Gamma_{np} \leq 0.9;$$

which indicates that neutron stimulated decay actually dominates the non-mesonic process, so simple models have significant problems in confronting the experimental numbers[18]. Other calculations of this ratio for various hypernuclear species do not consistently agree with the experimental measurements[19, 20]. It may be that quark effects are important, and reliable quark calculations would certainly be helpful, but precision measurements of the partial decay rates of non-mesonic hypernuclear decays are needed to determine the structure of the interaction Hamiltonian, and in

particular whether the $\Delta I = 1/2$ rule, which characterizes pionic decay and CP violation, also applies to non-mesonic decay of the hyperons. The experimental measurement of interest is the single and coincident nucleon emission spectrum of each species. An example of the proton and neutron emission spectra in the non-mesonic decay of two s-shell hypernuclei are shown in Figs. 1 and 2.

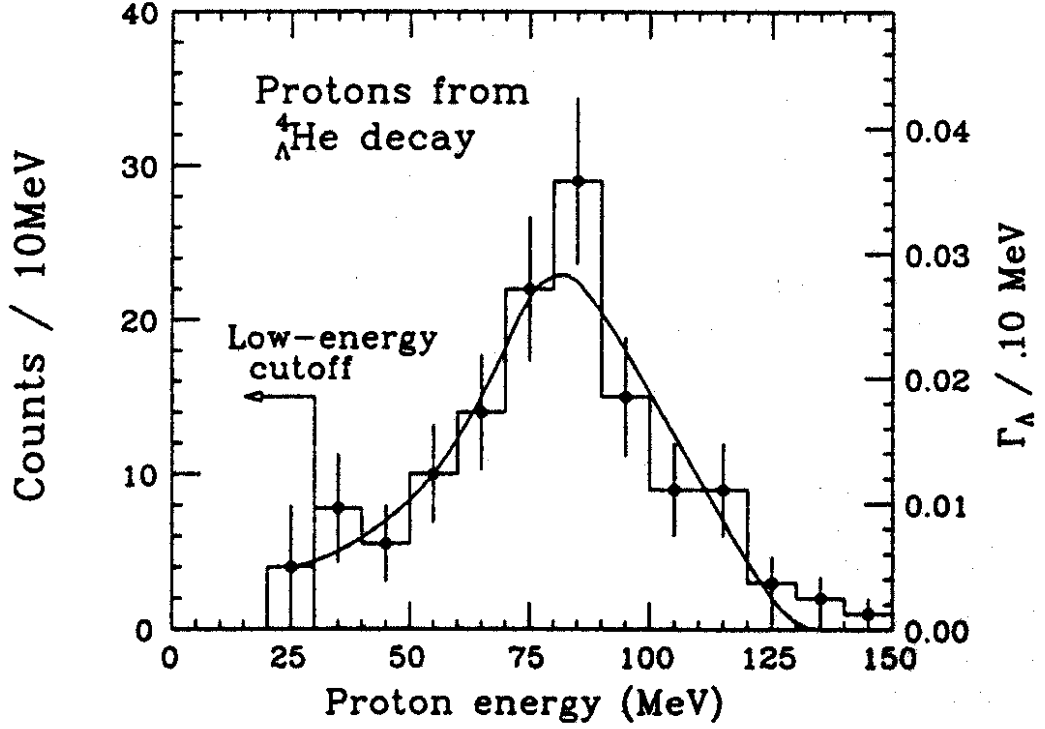


Figure 1: Experimental Spectrum of proton emission from the non-mesonic weak decay of ${}^4_{\Lambda}\text{He}$. The Curve is only to guide the eye

It is true that the more recent measurements of the shape of the NN coincidence NN seem more like the theoretical calculation[?]. However, there is a significant difference between the measurement of the asymmetry parameter of the decay. Decay asymmetries have been measured from the ${}^{12}_{\Lambda}\text{C}$ 1^- and the ${}^5_{\Lambda}\text{He}$ $1/2^+$ ground states. The ${}^5_{\Lambda}\text{He}$ measurement used the asymmetry of the mesonic decay to determine the polarization of the nuclear Λ . The best measurements of the asymmetry parameter are positive[?], but the theory produces only negative values, and it probably cannot be modified in its existing form to give a positive result, Table 2.

2.3 S-shell Hypernuclei

The s-shell hypernuclei can provide a significant testing laboratory for weak hypernuclear decay. Fig. ?? shows the level diagrams for the 3 s-shell hypernuclei. A global description of hypernuclear non-mesonic decay was first developed by Dalitz and collaborators in a series of papers [13, 14, 15]. Following this exposition, if we define the rate for $\Lambda\text{N} \rightarrow \text{NN}$ conversion in spin state $S=0,1$ as R_{NS} , where N is either a proton, p, or neutron, n, and R represents the spin and charge average for a specific hypernucleus, then for the decay of each of the s-shell hypernuclei;

$$\Gamma_{nm}({}^3_{\Lambda}\text{H}) = (1/8)\rho_3(R_{p1} + 3R_{p0} + R_{n1} + 3R_{n0})$$

Table 2: Comparison of Calculated Values of the Asymmetry Parameter, a_Λ to Experiment

Reference	${}^5_\Lambda\text{He}$	${}^{12}_\Lambda\text{C}$	Nucl. Matter
[?]			
OPE	-0.524	-0.397	
$\pi + K$	-0.509	-0.375	
[19]			
OPE			-0.192
OME			-0.443
[?]			
OPE	-0.441		
$\pi + K$	-0.362		
$\pi + K + DQ$	-0.678		
[?]			
OPE	-0.252	-0.340	
$\pi + K$	-0.509	-0.626	
OME	-0.675	-0.716	
Exp 160		-0.9 \pm 0.3	
Exp 278	0.24 \pm 0.22		
Exp 307		0.85 \pm 0.39	

${}^5_{\Lambda}\text{He} - \text{Neutrons}$

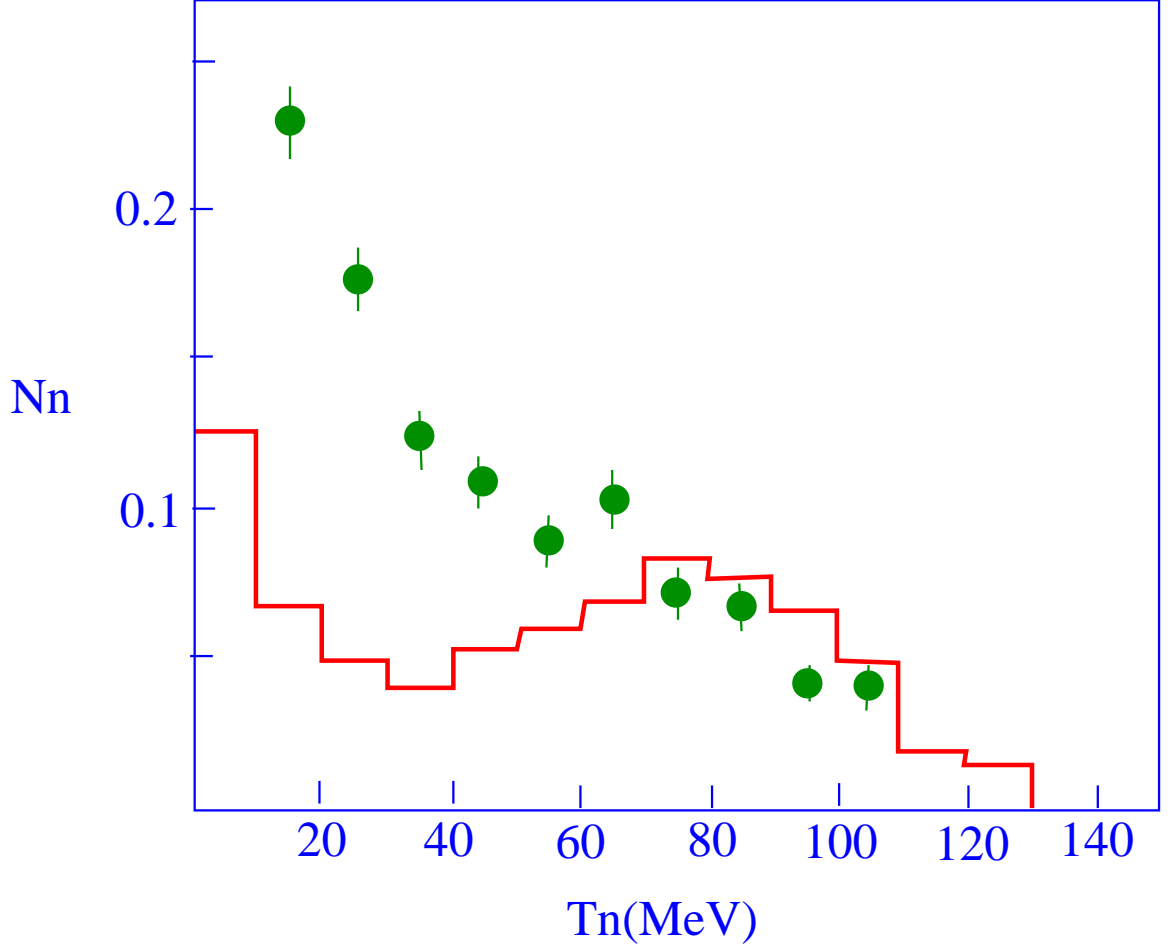


Figure 2: Experimental Spectrum of neutron emission from the non-mesonic weak decay of ${}^5_{\Lambda}\text{He}$. The Histogram is the theoretical calculation

$$\begin{aligned}\Gamma_{nm}({}^4_{\Lambda}\text{H}) &= (1/6)\rho_{(4^-)}(2R_{p0} + 3R_{n1} + R_{n0}) \\ \Gamma_{nm}({}^4_{\Lambda}\text{He}) &= (1/6)\rho_{(4^+)}(3R_{p1} + R_{p0} + 2R_{n0}) \\ \Gamma_{nm}({}^5_{\Lambda}\text{He}) &= (1/8)\rho_5(3R_{p1} + R_{p0} + 3R_{n1} + R_{n0}).\end{aligned}$$

Here the ρ factors represent the mean nucleon density at the position of the Λ in each nucleus, and are given by [14]:

$$\rho = (A-1) \int \rho_N(\vec{r}) \psi_{\Lambda}^2(\vec{r}) d^3r ;$$

where ρ_N is the nuclear density and ψ_{Λ} is the Λ wave function. It has been assumed in the past that the $A=4$ wave functions, and thus the ρ -factors, were the same for each of the two $A=4$ hypernuclear isotopes. The implications that they may be different has also been discussed [24].

For pure $\Delta I = 1/2$ decays, one finds that $R_{n0}=2R_{p0}$, as only $I=1$ final states are allowed. In addition, $R_{n1} \leq 2R_{p1}$, as both $I=0$ and $I=1$ final states are possible. Thus the $\Delta I=1/2$ rule implies:

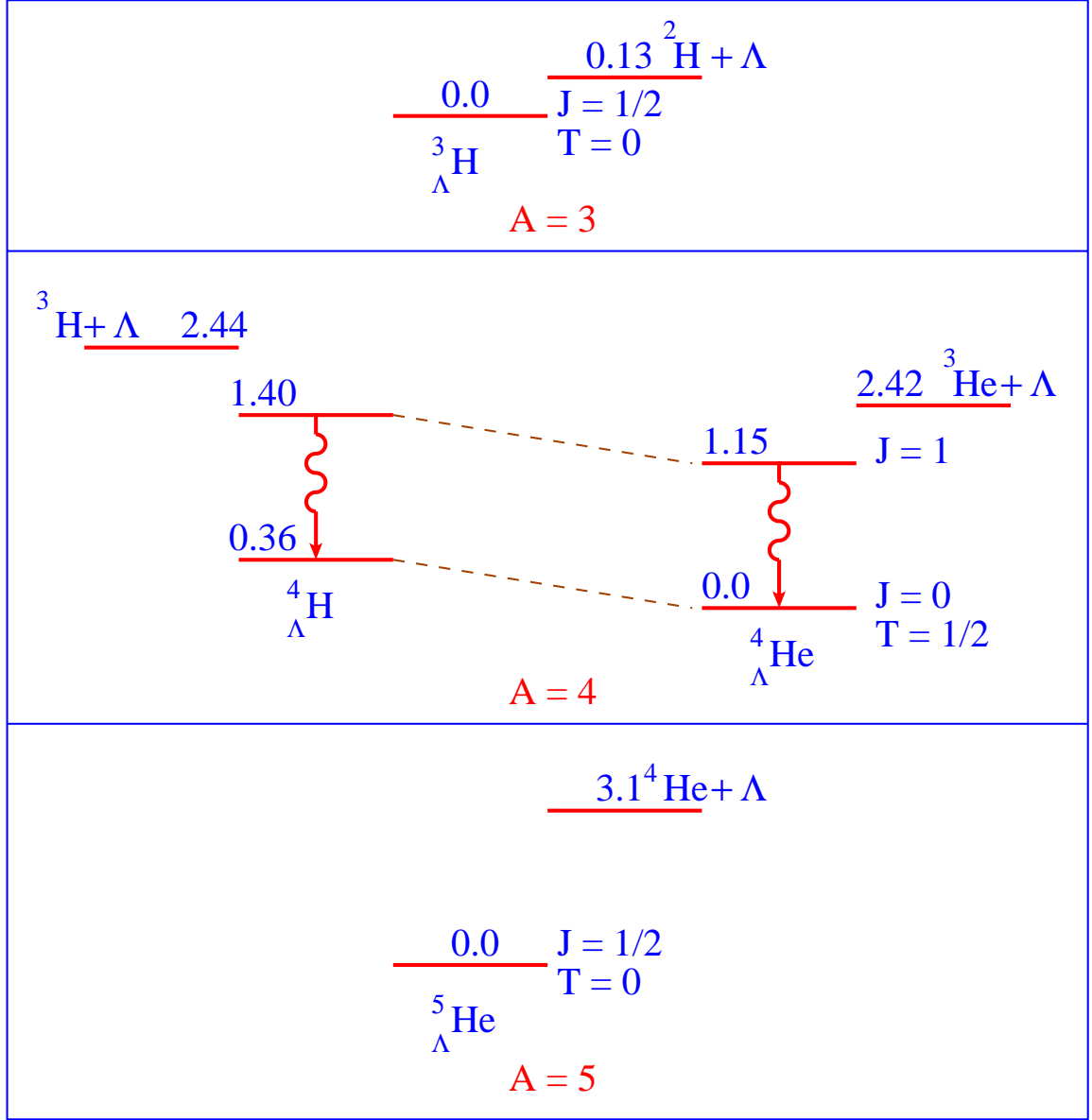


Figure 3: The Level Diagrams for S-shell Hypernuclei

$$r \equiv R_{n0}/R_{p0}=2.$$

A measure of the neutron to proton stimulated ratio for the four s-shell hypernuclear species then over-determines the ratio, r . To explicitly show the relations, we define the ratios:

$$\begin{aligned} \frac{\Gamma_{nn}({}^3_{\Lambda}\text{H})}{\Gamma_{np}({}^3_{\Lambda}\text{H})} &= \alpha_3[{}^3_{\Lambda}\text{H}] = \frac{R_{n1}+3R_{n0}}{R_{p1}+3R_{p0}} \\ \alpha_{(4^-)}[{}^4_{\Lambda}\text{H}] &= \frac{3R_{n1}+R_{n0}}{2R_{p0}} \\ \alpha_{(4^+)}[{}^4_{\Lambda}\text{He}] &= \frac{2R_{n0}}{3R_{p1}+R_{p0}} \end{aligned}$$

$$\alpha_5[{}^5_\Lambda\text{He}] = \frac{3R_{n1}+R_{n0}}{3R_{p1}+R_{p0}}$$

Written in matrix form these equations are:

$$\begin{pmatrix} \alpha_3 & 3\alpha_3 & -1 & -3 \\ 0 & 2\alpha_{(4-)} & -3 & -1 \\ 3\alpha_{(4+)} & \alpha_{(4+)} & 0 & -2 \\ 3\alpha_5 & \alpha_5 & -3 & -1 \end{pmatrix} \begin{pmatrix} R_{p1} \\ R_{p0} \\ R_{n1} \\ R_{n0} \end{pmatrix} = 0.$$

For a solution, the determinant of the matrix must vanish, which gives a relation between the values of α . Thus in terms of the ratio of most interest:

$$r = R_{n0}/R_{p0} = \frac{[4\alpha_3/\alpha_{(4-)} - 1]\alpha_{(4-)}\alpha_{(4+)}}{[4\alpha_{(4+)}/\alpha_3 - 1]\alpha_3} = \frac{\alpha_{(4-)}\alpha_{(4+)}}{\alpha_5}.$$

This shows the connection between the α s, but more importantly illustrates that the $\Delta I = 1/2$ rule can be tested by measurement of the proton to neutron stimulated decay rates in ${}^4_\Lambda\text{H}$ and ${}^4_\Lambda\text{He}$, and either ${}^3_\Lambda\text{H}$ or ${}^5_\Lambda\text{He}$. A measurement of the ratio in all the s-shell hypernuclei not only tests the $\Delta I=1/2$ rule but also the model. However, the measurement of α_3 is difficult as the ${}^3_\Lambda\text{H}$ hypernucleus decays almost exclusively by pion emission(95%) [17]. We note here that previous tests have not applied the ratios exactly as expressed above, so that these conclusions depended on the isospin difference in the nuclear overlap density, ρ , for the A=4 hypernuclei.

3 Physics to be Addressed

The experimental values for the s-shell hypernuclear decay rates are listed in Table 3. In this table the results from the more recent counter-experiments are shown in most cases, but a few examples of the older bubble chamber measurements are also given for comparison. A more complete review of the earlier data is given in the paper by Cohen [16]. In this table one can see that a measured value of α is only available for the ${}^4_\Lambda\text{He}$, and ${}^5_\Lambda\text{He}$ hypernuclei. Thus using only the model discussed in the last section, the $\Delta I = 1/2$ rule cannot be tested without additional information[?].

However by assuming that the nuclear densities of ${}^4_\Lambda\text{H}$ and ${}^4_\Lambda\text{He}$ are the same, and the density factors, ρ , cancel in forming the non-mesonic decay ratio;

$$\alpha_{(\pm)} = \frac{\Gamma_{nm}({}^4_\Lambda\text{He})}{\Gamma_{nm}({}^4_\Lambda\text{H})} = \frac{3R_{p1}+R_{p0}+2R_{n0}}{2R_{p0}+3R_{n1}+R_{n0}}.$$

This additional assumption can be used with the ratio, r , above to obtain;

$$r = \frac{[1 + \alpha_{(4-)}]\alpha_{(4+)}\alpha_{(\pm)}}{1 + \alpha_{(4+)}} = \frac{\alpha_{(4+)}\alpha_{(\pm)}}{1 + \alpha_{(4+)} - \alpha_5\alpha_{(\pm)}}.$$

As is evident from the above equation, a measure of $\alpha_{(4-)}$ is not required at the expense, of course, of some additional uncertainty in the model [24]. However the use of this equation is even more tenuous, as the measurement of $\alpha_{(\pm)}$ must then be determined by the ratio:

$$\alpha_{(\pm)} = \frac{\tau({}^4\text{H})Q^-({}^4_\Lambda\text{He})[1 + R_0 + Q^-]_{{}^4_\Lambda\text{He}}}{\tau({}^4\text{He})Q^-({}^4_\Lambda\text{H})[1 + R_0 + Q^-]_{{}^4_\Lambda\text{He}}};$$

where the factor, R_0 , is the ratio of $\Gamma_{\pi^0}/\Gamma_{\pi^-}$, and is not listed in Table 2. It has been measured for ${}^4_\Lambda\text{He}$, but not for ${}^4_\Lambda\text{H}$. However one can apply the $\Delta I = 1/2$ rule to the mesonic decays to obtain the constraint;

$$(R_0({}^4_\Lambda\text{H}))(R_0({}^4_\Lambda\text{He})) = 1/4.$$

Table 3: Experimental Parameters of S-shell Hypernuclear Decay in Terms of the Λ Free Decay Width[†]

	$\Gamma_{\Lambda}/\Gamma_{free}$	Q^- (Γ_{nm}/π^-)	$\Gamma_{nm}/\Gamma_{free}$	α	$\Gamma_{\pi^-}/\Gamma_{free}$	$\Gamma_{\pi^0}/\Gamma_{free}$
$^3_{\Lambda}H$	$1.13^{+0.19}_{-0.22}(1)$					
		0.4(2)				
	$2.05^{+0.42}_{-0.56}(3)$					
		0.0(4)				
$^4_{\Lambda}H$	$1.36 \pm 0.18(5)$				$1.00^{+0.18}_{-0.15}(5)$	
		$0.26 \pm 0.13(6)$	$0.29 \pm 0.14(6)$			
$^4_{\Lambda}He$	$1.07 \pm 0.11(7)$	$1.13 \pm 0.22(7)$	$0.20 \pm 0.07(7)$	$0.27 \pm 0.14(7)$	$0.17 \pm 0.3(7)$	
	$1.15 \pm 0.48(6)$	$0.56 \pm 0.09(6)$	$0.14 \pm 0.03(6)$	$0.40 \pm 0.15(6)$		
						$0.55 \pm 0.07(5)$
$^5_{\Lambda}He$	$1.03 \pm 0.08(8)$	$0.92 \pm 0.31(8)$	$0.41 \pm 0.14(8)$	$0.93 \pm 0.55(8)$	$0.44 \pm .11(8)$	$0.18 \pm 0.20(8)$

[†]Only most recent measurements are listed, for other values see J. Cohen
Prog. Part. Phys. 25(1990)139

1. G. Keyes, et al Nucl Phys B67(1973)269
2. V. Gorge, et al Nucl Phys 21(1960)599
3. G. Bohm, et al Nucl Phys B16(1970)46
4. B. Bhomik, et al, Phys Lett 3(1962)13
5. H. Outa, et al Nucl Phys A585(1955)109c
6. M.M. Block, et al Proc. Int. Conf. on Hyperfragments, St Cergue,1963,
CERN Report 64-1
7. V. J. Zeps and G. B. Franklin, Proc. 23rd Int. Symp. on Nucl. and Part. Phys.,
Universal Academy Press, Tokyo, 1995
8. J. J. Szymanski, et al, Phys Rev C43(1991)849

In this expression $R_{0\Lambda^4\text{He}}$ is measured to be 2.49 ± 0.34 [22], so $R_{0\Lambda^4\text{H}}$ is of the order of 0.1, and any error involving the use of the $\Delta = 1/2$ rule, so long as extreme deviations do not occur, is unimportant. These assumptions can provide a test of the $\Delta I = 1/2$ rule in non-mesonic decays [21]. One finds that;

$$\alpha_{(\pm)} \approx 0.7_{-0.2}^{+0.7}.$$

Then by substitution into the equation for r above, one finds that terms cancel in the denominator leaving a result with large error. The final value is [25];

$$r = \frac{0.20_{-0.12}^{+0.22}}{0.59_{-0.47}^{+0.80}} = 0.3_{-1.4}^{+2.4},$$

which simply states that, because of the large errors, no meaningful test has been made. These errors come from uncertainties in the measured quantities, and in particular, in the way they are compounded in the above expressions.

If one uses the value obtained from the $\Delta I = 1/2$ rule, $r=2$, and also the connection between r and the α s given above, a value of $\alpha_{(4-)} \approx 7.0_{-5}^{+15}$ is predicted. This quantity should be directly measurable to at least a 50% error as is the case for the other values of α in the s -shell hypernuclei. If it can be measured with an accuracy of better than 50%, then the error in r would be dominated by the other uncertainties. If $r \approx 0.3$ as suggested above, a measurement of the α s to 50 % accuracy would clearly bound r away from 2, showing a violation of the $\Delta I = 1/2$ rule.

If in addition, the non-mesonic decay rate from ${}^3_{\Lambda}\text{H}$ were also measured, the hypernuclear model could be tested. Assuming the validity of the $\Delta I = 1/2$ rule, one can predict that, $\alpha_3 \approx 2.2_{-1.6}^{+3.3}$. While applying α_3 to obtain r is not as sensitive as using α_5 , it does provide a consistency check in the case where r is determined by other means. In any event, a measure of the non-mesonic decay of the ${}^3_{\Lambda}\text{H}$ hypernucleus is difficult but inherently interesting, as it is the lightest bound, and most easily calculated Λ -nuclear system. Although it is the goal of this proposal to measure the non-mesonic decay rates of ${}^4_{\Lambda}\text{H}$, we also express the intent to later address measurements of α for other the s -shell hypernuclei to provide a consistent set of all the α values.

4 Experimental Arrangement

If photoproduced, the experiment will use a 40cm long 3cm diameter liquid ${}^4\text{He}$ target. If electro-produced, the luminosity sets the beam current times target thickness to be $\approx 10^{34}$. Detection of the scattered electron in the case of electroproduction uses a geometry discussed below. In both cases (either real or nearly real photons) the photon energy will be approximately 1500 MeV, which is near the peak in the elementary photoproduction cross section, $\gamma p \rightarrow K^+ \Lambda$. We will use an 1800 MeV electron beam, detecting bremsstrahlung or reaction electrons at approximately 300 MeV [?, ?]. The proposed electroproduction geometry was successfully used in E89-09 to observe the first electroproduction of hypernuclei. A typical experimental arrangement is shown in Fig. 4.

For electroproduction, the electrons tagging the virtual photons remain essentially at zero degrees. This permits the use of the large virtual flux that is produced at very forward angles, Fig. 5. Fig. ?? shows that for our proposed geometry, which has a 100 MeV virtual photon momentum bite at approximately 1500 MeV, one would expect about 3×10^{-4} photons per incident electron. A major advantage of using the ≈ 0 deg. virtual flux is the very small acceptance required for the electron spectrometer, $\approx 3 \times 10^{-4}$. A polar angle acceptance of 10 mr captures almost 40% of the virtual photon flux in this momentum bite. For a beam of 1 μA , we would tag approximately 1.8×10^9 virtual photons. This flux of tagged photons is nearly on the mass shell (*ie the photon energy is much greater than the absolute value of the photon mass*, so they can be treated as real for the purposes of cross section calculations. In the case of photoproduction we would tag approximately 10^8 real photons. In either case, the limiting luminosity in CLAS would be 10^{34} . In the case of real photons a longer target can be used to provide the maximum luminosity.

For electroproduction, scattered electrons of approximately 300 MeV remain within a small angular

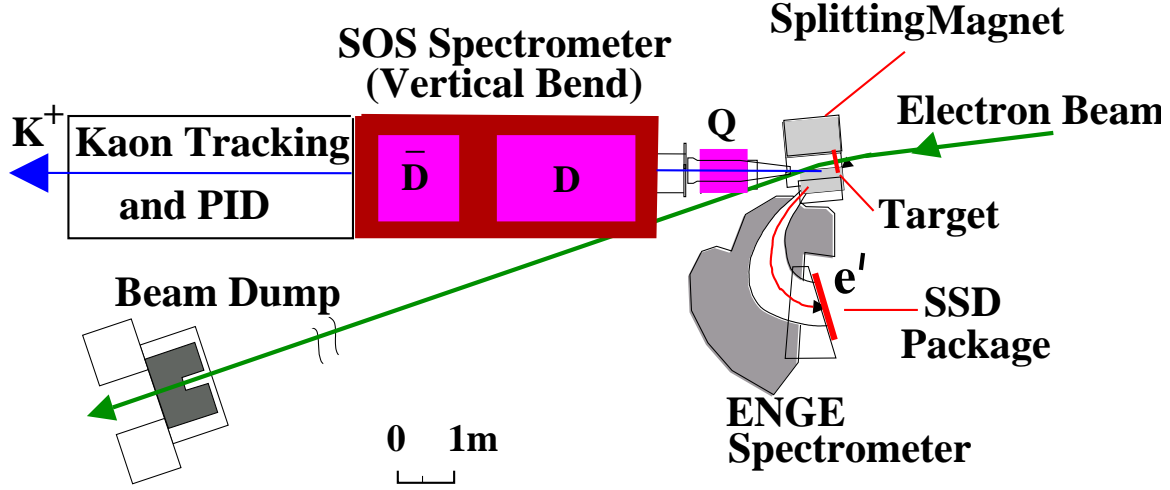


Figure 4: Experimental Layout for the Hypernuclear Experiment in HallC. The same electron tagging system would be used while the kaons would be detected in CLAS for the ${}^4_{\Lambda}\text{H}$ measurement

cone of polar angle ≤ 10 mr, exiting CLAS and entering into the ENGE spectrometer system. A short quadrupole element can be used to assure that the 300 MeV scattered electrons are accepted by the 0 degree magnet and the spectrometer. A similar geometry was used in the successful E89-09 experiment[?] to observe the electroproduction of ${}^1_{\Lambda}\text{B}$ hypernuclei. The momentum resolution of this system would be some 3×10^{-3} , which is more than sufficient. We also note that because of the small angular acceptance, only position along the ENGE focal plane is adequate to obtain this resolution. Tracking is not necessary, nor given the count rate, is it practical. In the case of photoproduction, the existing CLAS tagged photon beam would be used, but resolution of at least $\delta p/p \leq 0.01$ is required.

Both charged and neutral particles from decays of the ${}^4_{\Lambda}\text{H}$ hypernucleus will be detected by scintillation walls. The charged particles will also be tracked by the wire chambers in the CLAS detector and their momentum determined.

A combination of time-of-flight, energy loss, and curvature can distinguish pions from protons. Neutrons are observed by an array of thick scintillation bars, covered by veto scintillators, Fig. ???. Neutron detection efficiency is not well explored in CLAS, but appears to be between 3-10 %. We choose 5% for the rate calculations.

5 Particle Identification

A new **KAon Tracker** in the **Z** direction, **Katz**, is to be used to identify and detect forward going kaons. It is described in detail in the appendix. Katz has a toroidal magnetic field surrounding the beamline just downstream of the target. This field would be approximately 1.3T and 20 cm long. It would bend the 1.2 GeV/c kaons produced at small angles by ≈ 4 deg. to larger angle trajectories. In this way, kaons produced at angles > 7 deg would reach the drift chambers in CLAS. Behind this region of magnetic field, is a Ring Imaging Cerenkov Detector, RICH. The RICH detector covers an annular ring of approximately 5-15 degrees, with the inner radius of the annulus of about 5 deg. Kaons bent at a sufficiently large angles will enter the forward portion of the CLAS drift chamber system. This provides an approximate 5 deg. polar angle bite which is acceptable for hypernuclear production as the angular distribution is strongly peaked in the forward direction. A number of forward kaons are detected in Katz but are not bent sufficiently to enter the CLAS drift chambers, however, Katz will also contain a set of silicon strip detectors surrounding the target and tracking detectors behind the field region so that a momentum measurement is possible for the full annular region of the detector, albeit with poorer resolution. However even these kaons will be

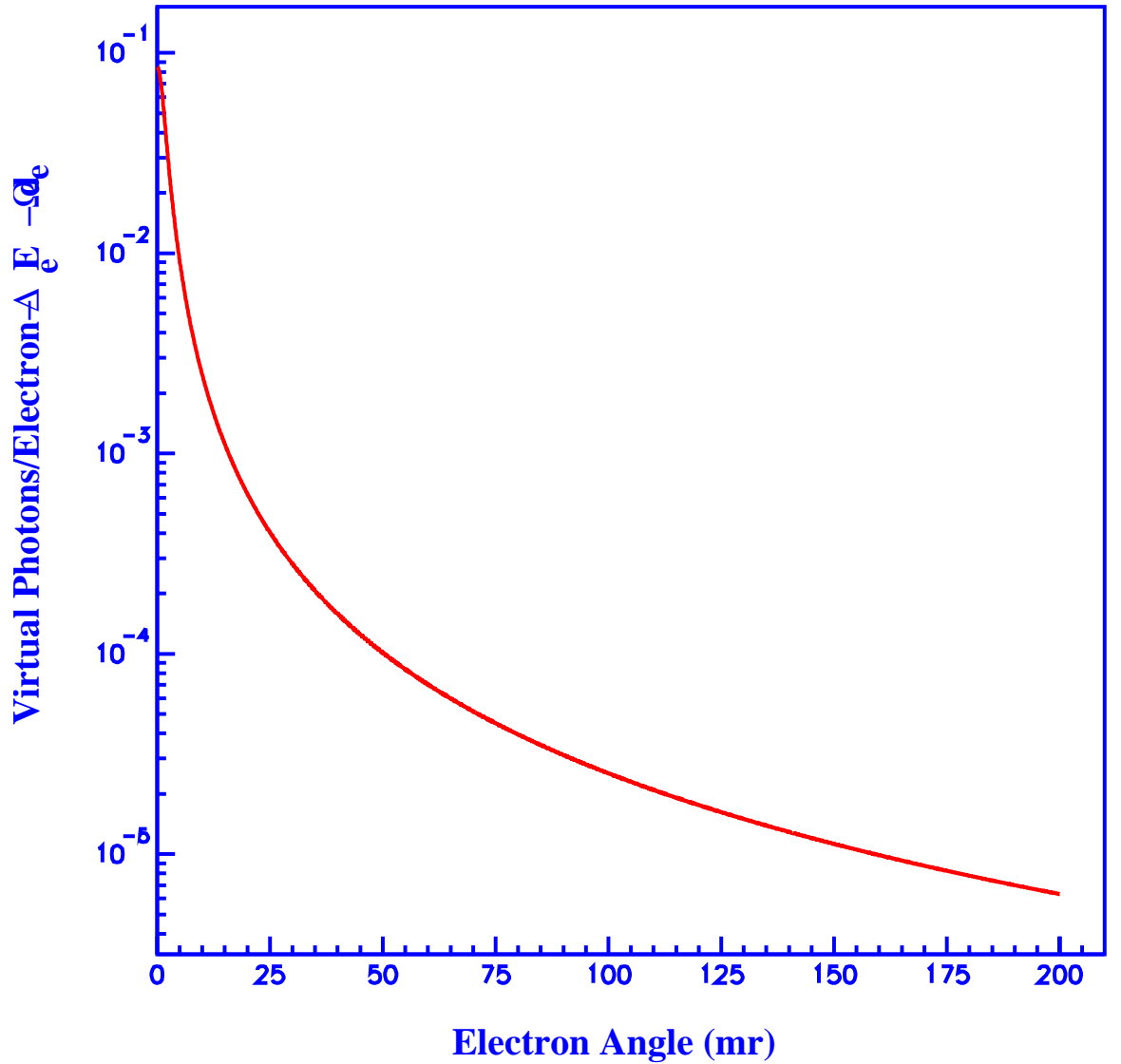


Figure 5: The Virtual Flux Factor for 1800 MeV Electrons as a Function of Polar Angle for Approximately 1500 MeV Photons

useful for the decay measurement, and the wider acceptance will extend the flexibility of Katz.

6 Count Rate Estimates

The ${}^4_{\Lambda}\text{H}$ hypernuclei will be produced in the ${}^4\text{He}(\gamma, K^+){}^4_{\Lambda}\text{H}$ reaction. Thus a fractional branching rate measurement has four distinct components: 1) photon production, 2) hypernuclear tagging, 3) hypernuclear decays, and 4) data acquisition.

Photon Production

Photon production involves the number of bremsstrahlung or virtual photons photons tagged by the (e, e') reaction. Bremsstrahlung at zero degrees can be estimated from the equation;

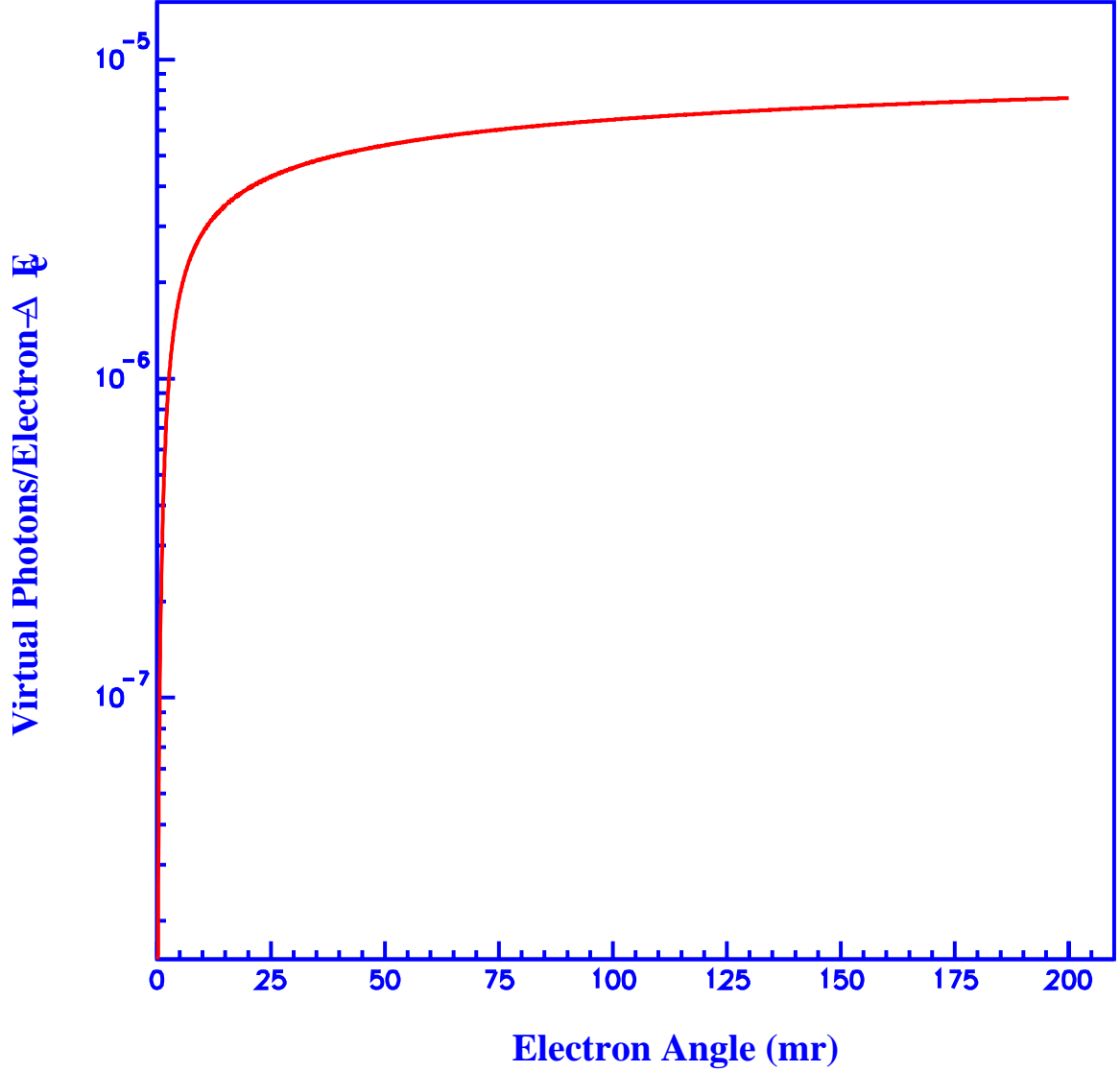


Figure 6: The Virtual Flux Factor Integrated for a 1800 MeV Electrons Integrated over the Electron Solid Angle as a Function of Polar Angle for 1500 MeV Photons

$$dN_e = (\chi/\chi_0) (dE_e/E_\gamma) N_e$$

Here χ/χ_0 is the target thickness in radiation lengths, dE_e is the energy acceptance of the tagging spectrometer, and E_γ is the energy of the photon, $(E_e - E'_e)$. Thus one expects to reach a luminosity of 10^{34} when the effective luminosity for the reaction of interest is $(100/1800)10^{34} = 5.5 \times 10^{32}$. The ${}^4\text{He}(\gamma, K^+) {}^4_\Lambda\text{H}^*$ cross section is calculated?? to be 50×10^9 nb/sr. The reaction is predominately to the excited 1^+ state at 1.04 MeV. The Kaon solid angle is estimated to be about 45 msr. This produces a tagged hypernuclear formation of;

$$Tagged/s = (3.3 \times 10^{32})(50 \times 10^{-33})(0.045) = 1.1s^{-1}$$

All numbers for the decay branching fractions are either measured, or are best estimates based on the literature. Assuming the $\Delta I = 1/2$ rule is valid, the proton branch is determined using the neutron measurement in ${}^4_\Lambda\text{He}$. If the $\Delta I = 1/2$ rule is violated, the proton fraction should be larger, so this is a conservative estimate of the number of observed protons. Furthermore, we expect that we may be able to increase the solid angle coverage for the protons as the experimental details are

Table 4: Expected counts for decay of ${}^4_{\Lambda}\text{H}$

Assuming 700 hours of production: $\Gamma_{\Lambda}/\Gamma_{free} = 1.36$ Total ${}^4_{\Lambda}\text{H}$ production: 2.8×10^6		
Particle Decay mode	Per s	Expected 700 Hours
π^-	0.8	1.2×10^6
Protons	0.03	4.6×10^4
Neutrons	0.3	2.0×10^4
Proton-Neutrons	8.6×10^{-4}	2.2×10^3
Neutron-Neutrons	3.8×10^{-4}	9.6×10^2

optimized. From the decay tables and theoretical estimates we expect the following;

$$\Gamma_{\Lambda}/\Gamma_{free} = 1.36 ;$$

$$\Gamma_{nm}/\Gamma_{\pi^-} = 0.26 ;$$

$$\Gamma_{nm}/\Gamma_{free} = 0.29 ;$$

$$\Gamma_{nm}/\Gamma_{\Lambda} = 0.21 ;$$

$$\Gamma_{pi^-}/\Gamma_{\Lambda} = 0.74 ;$$

$$\Gamma_p/\Gamma_n = 0.13 ;$$

$$\Gamma_p/\Gamma_{nm} = 0.12 ;$$

We apply a proton detection efficiency of 0.6 and a neutron detection efficiency of 0.5. This results in the rates given in Table 4.

The expected number of tagged events is listed in Table 4.

7 Expected results

We expect to measure the ratio of proton to neutron stimulated non-mesonic decay, α , in the ${}^4_{\Lambda}\text{H}$ s-shell hypernucleus to an uncertainty of less than 50%. When combined with previous results in other s-shell hypernuclei, this will provide the first definitive test of the $\Delta I = 1/2$ rule in non-mesonic hypernuclear decay. We note that $\alpha_{(4^-)}$ would be quite large ($\approx 7.$) if the $\Delta I=1/2$ rule applies, as compared to $\alpha_{(4^+)} \approx 0.27 \pm 0.14$. Thus we expect to obtain a result which should have a smaller error than our previous measurement.

However even a measurement with a 50% error should provide a significant test of the $\Delta I = 1/2$ rule. If successful, we would then propose to measure the non-mesonic branching ratios in the decay of ${}^3_{\Lambda}\text{H}$.

A KATZ, a KAon Tracker in Z direction for CLAS

The present CLAS detector setup has four major limitations, which are all addressed simultaneously with a new detector design presented in this paper. Those missing features are the capability to measure the four-momentum of charged particles in forward and backward direction at small angles with respect to the beam line, the separation of charged π and K with excellent signal to background ratio for individual tracks without the aid from other measurements, the lack of a trigger for events with charged kaons at small angles, and the precision measurement of the particle energy with an accuracy of only a few MeV. The components of the new setup are; 1) a scintillator plane used as start counter, 2) a system for measuring charged particle trajectories, and 3) a RICH. The new detector fits into the space between the fixed target and the CLAS drift chamber region number 1.



Figure 7: K^ATZ at work [UNKNWN].

*Die Katze ist das einzige vierbeinige Tier, das dem Menschen eingeredet hat, er müsse es erhalten,
es brauche aber dafür nichts zu tun.*¹

Kurt Tucholsky

¹The cat is the only four-legged animal that talked people into nourishing it without doing anything in return.

B Introduction

KATZ stands for “KAon Tracker in Z direction”. The primary motivation for this new design of a detector set is to support new strange particle physics at medium and high energy with the CEBAF Large Acceptance Spectrometer (CLAS) [CLAS03]. New experiments include “A Study of the Weak Decay of the S-Shell Hypernucleus, ${}^4_\Lambda\text{H}$ and the $\Delta I = \frac{1}{2}$ Rule” [HUNG04], the measurement of the cross section and various polarization observables of the hyperon ground state [SCHU04] and excited state [JUEN01] production at very small and very large polar angles, the measurement of kaon resonance [?], and cascade and Ω^- production [?].

The primary purpose of the new set KATZ is the detection and measurement of charged kaons within a predetermined kaon energy range at small angle with respect to the beam line. KATZ enhances the separation of charged π and K with a Ring Image Čerenkov (RICH) detector. The expected energy range of the kaons determines the refractive index. The refractive index, and consequently the optimum energy range for kaon detection, can be customized by exchanging the Čerenkov material. An important feature of KATZ is its ability to trigger on charged kaons. This makes it an important tool for future strange particle experiments. A fast particle identification logic for the separation of pions and kaons facilitates the inclusion of KATZ in the second level trigger of CLAS for dedicated experiments which require the detection of kaons at small polar angle and a good signal to background ratio. KATZ comes with its own start scintillator. This start counter replaces the usual CLAS start counter (ST) for photoproduction runs. This not only reduces the energy loss for particles going into the CLAS drift chambers (DC), but also allows the inclusion of a vertex detector in the area prior occupied by ST for better vertex measurement and detection of particles with low momentum at polar angles between 15° to 165° .

Although the primary purpose of KATZ focuses on the detection of kaons, it is very well suitable for the identification and measurement of charged pions and protons over a wide energy range at small polar angles. This makes it a universally adaptable viable detector. The total amount of material in the path of particles is comparable with the amount from the CLAS drift chambers. Since we already know that we can utilize the CLAS electromagnetic shower counters (EC and LAC) behind the DC, it would be justifiable to assume that a calorimeter downstream in forward direction for small polar angles [?] could coexist with KATZ. For example experiments with kaon resonances decaying into a charged kaon and neutral pion with subsequent 2-gamma decay would be feasible with KATZ having a calorimeter downstream.

Another interesting aspect of KATZ is the possibility to install not only one set in forward direction, but also another, identical set in backward direction. With both sets installed CLAS will allow measurements with a polar angle in the laboratory systems between 2° and 178° . This new feature dramatically reduces the size of the gaps in the current CLAS data.

There are various open questions about other applications of KATZ. These questions will be addressed in the near future. This paper assumes photoproduction, but electroproduction presents an important field of application. Currently under investigation is also the possibility to separate charged pions and muons with KATZ. Muon physics with CLAS is an interesting complementary program.

C Units

For KATZ only units defined by the metric system based on the International System of Units (Système International d’Unités, SI) and derived SI units are used. For practical reasons a conversion by an integer number n to the power of 10 might be acceptable, for example if needed for machine-production. All intermediate changes have to be documented.

For the GEANT simulation and analysis software we use cm, s, GeV and g only [GEANT3]. There is no practical reason to switch factors in the software, because the computers can perfectly handle any numbers with the given units. For example switching between GeV and MeV results in no improvement, but does introduce new stumbling blocks.

D Design

The design of KATZ determines its performance and application. The new design needs to address various shortcomings of CLAS and fulfill all requirements of the experiments for which it is going to be used. As an example, “A Study of the Weak Decay of the S-Shell Hypernucleus, $^4_\Lambda\text{H}$ and the $\Delta I = \frac{1}{2}$ Rule” [HUNG04] needs be supported by KATZ.

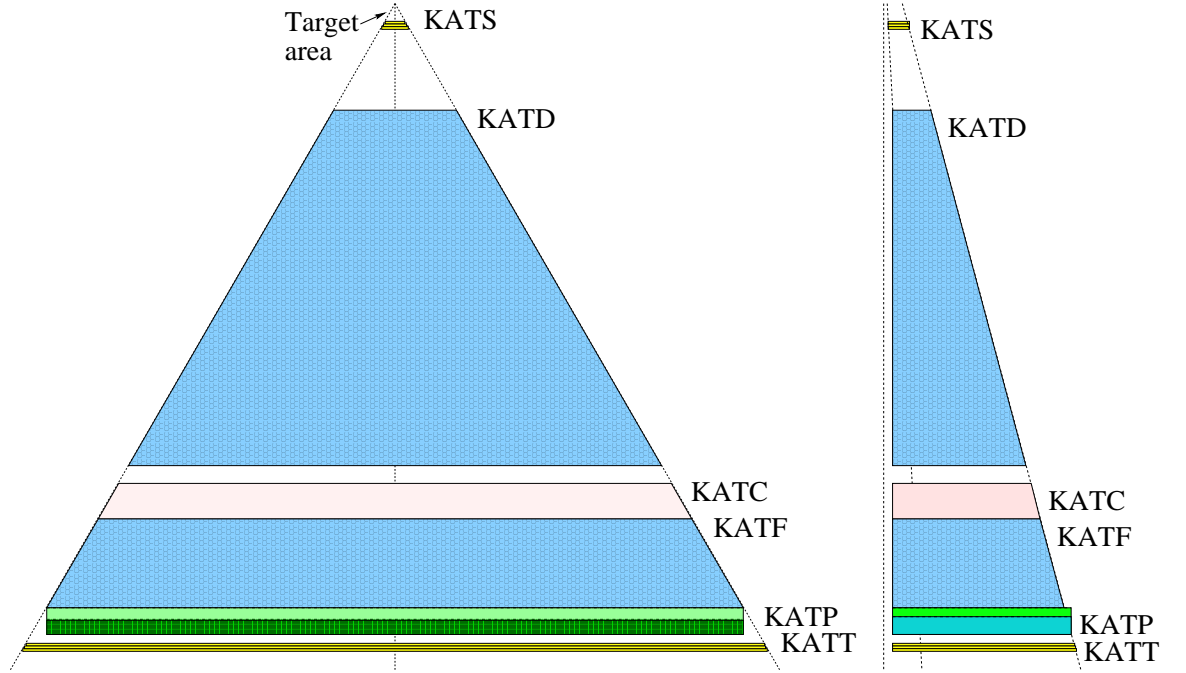


Figure 8: A schematic of KATZ, left panel showing a topview of all six KATZ components (KATS, KATD, KATC, KATF, KATP and KATT) for one CLAS sector, right panel show a cross section of KATZ.

KATZ is a set of detectors and volumes filled with material. It consists of the following six components, as also illustrated in Fig. 8.

1. KATS, a scintillator detector for the start signal of a time-of flight measurement, level 1 trigger
2. KATD, a long drift chamber
3. KATC, Aerogel-Čerenkov material
4. KATF, a short drift chamber filling the space between KATC and KATP
5. KATP, a solid CaF_2 plane attached in front of a fast multi-wire proportional chamber, level 2 trigger

These six detector and volume names are used in the newly developed GEANT simulation of KATZ within the existing CLAS GEANT simulation known as GSIM. KATZ is also the name used in the GEANT simulation for the entire *set*.

The left panel of Fig. 8 shows the topview for one sector and the right panel shows the cross section of KATZ. The schematic in the left panel reproduces the 60° angle for each of the six CLAS sectors. The right panel of Fig. 8 shows the two opening angles of a track coming from the target with respect to the beam line. The assumed distance between the downstream end of the target and KATZ is 10 cm. With an outer diameter for the beam line of 1 cm this leaves a minimum opening angle of 2° , assuming no contribution from a magnetic field and measured from the back end of the target

cell. From the front KATZ looks like a hexagon. As this is not circular the average opening angle is slightly larger than 2° . However, particles originating from a vertex further upstream, within the target cell, will still be detected by KATZ at an even small angle. The maximum opening angle is set to be 15° . The space beyond 15° is covered by the CLAS drift chambers (DC) and time-of-flight scintillators (SC). The KATZ detectors downstream cover even a smaller minimum opening angle. This is necessary because some particles, depending on the sign of their charge, will be bent towards the beam line by the magnetic field in the area of the front drift chamber KATD. The two schematics in Fig. 8 do not show the magnet.

The location of each KATZ component is listed in table 5. The total depth of KATZ is 71 cm. KATZ fits into the space between the CLAS fixed target at its nominal position and the first region of the CLAS drift chamber (DC). The nominal distance between the target and the first KATZ detector, namely KATS, is 10 cm.

Component	begin	end
KATS	0.0	1.0
KATD	10.0	50.0
KATC	52.0	56.0
KATF	56.0	66.0
KATP	66.0	69.0
KATT(if necessary)	70.0	71.0

Table 5: Relative position (cm) of each KATZ component in Z-direction (along the beam line).

Six identical assemblies cover all six sectors of CLAS. The support structure and connecting parts cover only the area of the CLAS main magnet torus. This means KATZ does not limit the acceptance of any other CLAS detector. The current design assumes that the KATZ start counter (KATS) is sufficient to replace the traditional CLAS start counter (ST) used in photoproduction. The space in the ST area can now be used for a vertex or low momentum detector to cover the polar angle range between 15° and 165° .

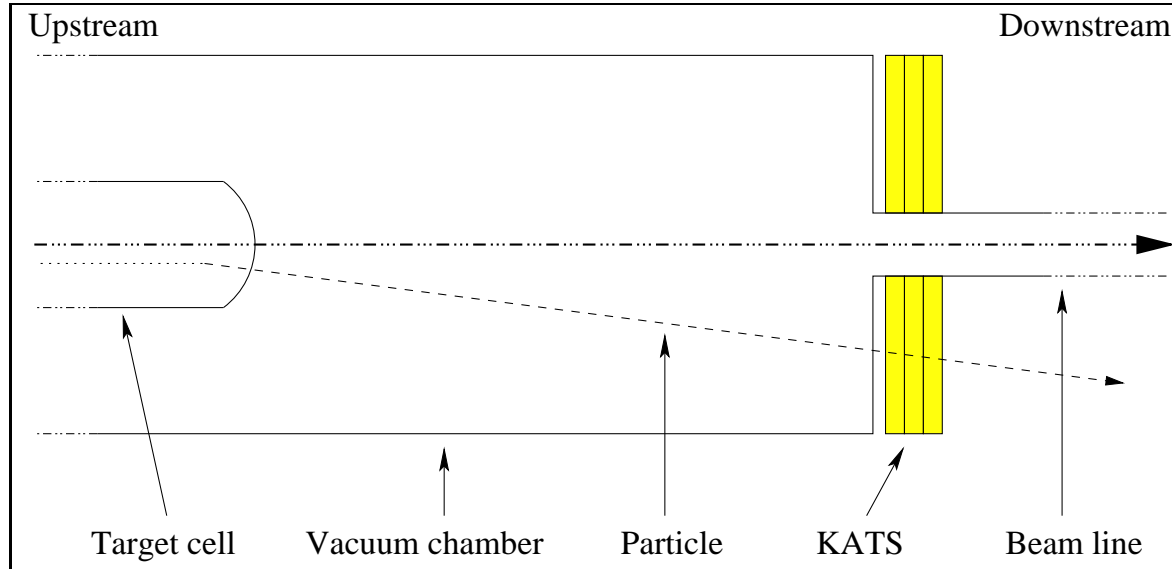


Figure 9: A new target cylinder to operate KATZ.

A new optimized target cylinder is required to operate KATZ. It is shown in Fig. 9. The wall of the vacuum chamber has been extended so that it covers completely the front of the start counters

KATS. This minimizes the angle through which all particles in forward direction traverse the back end of the vacuum chamber. The goal is minimize the probability that particle travel parallel through the wall of the vacuum chamber or beam line. This optimization will help to minimize multiple scattering and energy loss for particles going in forward direction.

D.1 RICH detector

The most important component of KATZ is a Ring Image Čerenkov (RICH) detector. Particles may interact with the RICH detector and produce Čerenkov light. The Čerenkov light is emitted at a specific angle. This angle depends on each particle's speed β . The emitted Čerenkov light forms a ring. The radius of this ring is measured by the RICH detector.

The RICH detector of KATZ consists of two parts. The first one is KATC, a block of Aerogel-Čerenkov material which is used as radiator. The second part is KATP, a fast multi-wire proportional chamber (MWPC) with a CaF_2 plane directly in front of the MWPC. KATP is a photon detector. The distance between the Aerogel-Čerenkov material and the fast multi-wire proportional chamber is 10 cm. This space is used to project the Čerenkov light cone coming from the interaction of the kaons and pions with the Aerogel-Čerenkov material onto the fast multi-wire proportional chamber KATP, after converting the Čerenkov light into electrons by the CaF_2 plane. The space between KATC and KATP is filled with a short drift chamber (KATF).

D.1.1 Čerenkov light emission and measurement

Two components are needed for a RICH detector, namely a radiator and a photon detector. The purpose of the radiator is to produce Čerenkov light when a charged particle traverses the radiator under certain circumstances, while the photon detector is used to detect the projection of the Čerenkov light.

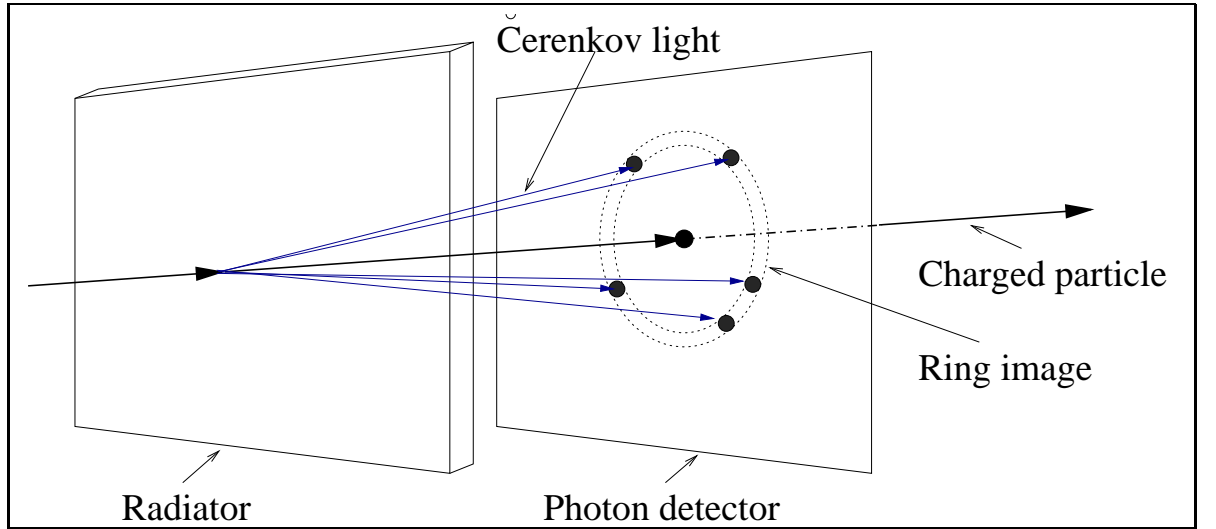


Figure 10: Čerenkov light emission from interaction of a charged particle with a radiator and the projection of the Čerenkov light as ring image onto a photon detector.

Čerenkov light emission from the radiator and its subsequent projection onto the photon detector are illustrated in Fig. 10. A charged particle with mass m , charge q , momentum p , and velocity

$$\vec{\beta} = \frac{\vec{v}}{c} \quad (1)$$

hits a radiator. The material of the radiator has a refractive index n , whereby $n = n(\lambda)$ depends on the wave length λ . In the medium the speed of light c_n is $c_n = \frac{c}{n}$. A particle traversing the medium with

$$\beta > \frac{c_n}{c} \quad (2)$$

causes an asymmetric polarization with a resulting dipole moment, which then emits Čerenkov light at an angle

$$\Theta_{\check{C}} = \arccos \frac{1}{n\beta}. \quad (3)$$

The Čerenkov light is projected onto the photon detector at a distance d with a ring image radius

$$r = d \tan \Theta_{\check{C}}. \quad (4)$$

The radiator has a thickness $\Delta d > 0$. Therefore the ring image will cover the area between r and $r' = (d + \Delta d) \tan \Theta_{\check{C}}$, with $r' > r$.

The number of emitted photons N_{photon} can be calculated with

$$\frac{dN_{photon}}{dd} = 2\pi\alpha q \int_{\lambda_1}^{\lambda_2} \left(1 - \frac{1}{n(\lambda)^2\beta^2}\right) \frac{d\lambda}{\lambda^2}, \quad (5)$$

whereby $\alpha = \text{fine structure constant} = \frac{1}{137}$. Assuming $n(\lambda) = \text{const}$ and $|q| = 1$, we get

$$N_{photon} = 2\pi\alpha d \left(1 - \frac{1}{n^2\beta^2}\right) \left(\frac{1}{\lambda_2} - \frac{1}{\lambda_1}\right). \quad (6)$$

The number of emitted photons is quite limited and is typically about 20. These few photons are distributed over the entire ring image area and have to be detected with sufficient spacial resolution. Ultimately only a few dots will be detected. These dots have to be used to calculate the ring radius. With KATZ we use KATP, a CaF_2 plane followed by a multi-wire proportional chamber, as photon detector. The conversion probability and detection efficiency is significantly smaller than 1. Therefore only a few dots make up the ring image. But, fortunately the initial charged particle will also interact with the multi-wire proportional chamber and the efficiency of detecting this dot is practically 1. Therefore the center of the ring image is always known, assuming that at least 2 dots on the ring are also detected. This helps greatly to locate and evaluate the ring image.

D.1.2 Aerogel-Čerenkov material KATC

A filled box (KATC) of Silica Aerogel Čerenkov material is used in KATZ to produce the Čerenkov light with charged pions and kaons. It is important to notice that the KATZ design calls for a refractive index large enough for kaons to produce Čerenkov light. The KATZ Čerenkov detector is not configured as Threshold Čerenkov Counter. Instead we expect a ring image from pions and kaons. The separation takes place when the radius of the ring image, the measured time-of-flight and the measure 3-momentum are combined. The cross sections for π -production are significantly larger than the cross sections for K-production. For a better signal-to-background ratio we need to have a positive identification of the kaons. If we would set the refractive index so low that the kaons would not produce Čerenkov light and only veto on pions, then the pileup of misidentified

pions would end up as false kaons due to the error of momentum and time-of-flight measurement and the limited efficiency of the RICH detector. Protons with a momentum below 1.5 GeV/c will not produce any Čerenkov light with the planned range of the refractive index. Therefore protons with low momentum cannot be misidentified as kaons since we require a image of the Čerenkov light in the RICH detector. Protons with high momentum can be separated from kaons the same way we separate kaons and pions. The refractive index of Silica Aerogel can be adjusted to be between $n > 1.002$ and $n < 1.2$ [AERO98]. For a particular experiment the Silica Aerogel material with the proper refractive index n needs to be prepared and installed. Although the detector works over a broad momentum range, it is important that the refractive index is being optimized.

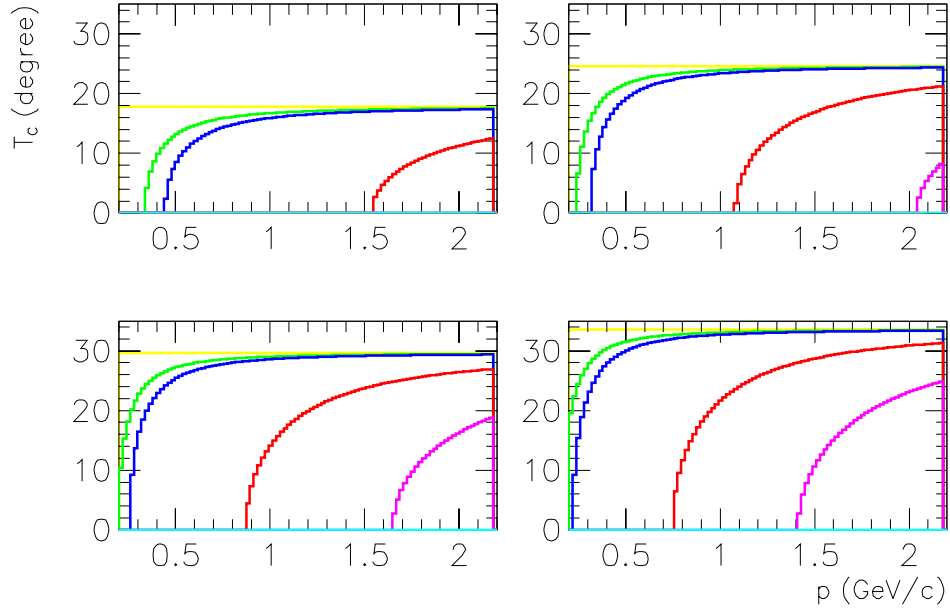


Figure 11: Čerenkov light emission angle Θ_C vs. particle momentum p , with refractive index $n = 1.05$ (top left), $n = 1.10$ (top right), $n = 1.15$ (bottom left), and $n = 1.20$ (bottom right); each for e^\pm (top, yellow curve), μ^\pm , π^\pm , K^\pm , p/\bar{p} , and d (bottom, cyan curve, *not seen*).

The Čerenkov light emission angle Θ_C is an important quantity for the particle separation. When optimizing the refractive index n we need to make sure that Θ_C is different within the accuracy of the multi-wire proportional chamber for the particles which need to be separated, while at the same time sufficient margin for the accepted particle momentum range is available. In any case n has to be large enough that Čerenkov light is being emitted for all particles to be detected at the expected particle momentum range. The Čerenkov light emission angle Θ_C is plotted versus the particle momentum p for the refractive index $n = 1.05$, $n = 1.10$, $n = 1.15$, and $n = 1.20$ in Fig. 11. Each plot includes the six most important charged particle at CLAS, namely e^\pm , μ^\pm , π^\pm , K^\pm , p/\bar{p} , and d . These plots are used to determine the refractive index.

For 1.2 GeV/c kaons, as expected in [HUNG04], the aerogel of the Čerenkov detector needs to have a refractive index of about $n = 1.15$. At $n = 1.10$ the angle Θ_C for kaons is only 5° , which corresponds to a ring radius of only 0.9 cm. This is too small. Also the margin for the kaon momentum is very small. Below a kaon momentum of 1.1 GeV/c there will be no Čerenkov light emission at $n = 1.10$. For $n = 1.05$ the minimum momentum of the kaon has to be at least 1.5 GeV/c, which makes it completely impossible to detect kaons with a momentum of 1.2 GeV/c. At a refractive index, for example $n = 1.2$, we find that the difference between the angle Čerenkov light emission angle $\Theta_C(\pi)$ for pions and the angle $\Theta_C(K)$ for kaons decreases rapidly. A good compromise for all criteria is achieved with $n = 1.15$.

Figure 12 shows the minimum momentum p_{\min} as a function of the refractive index n for e^\pm , μ^\pm ,

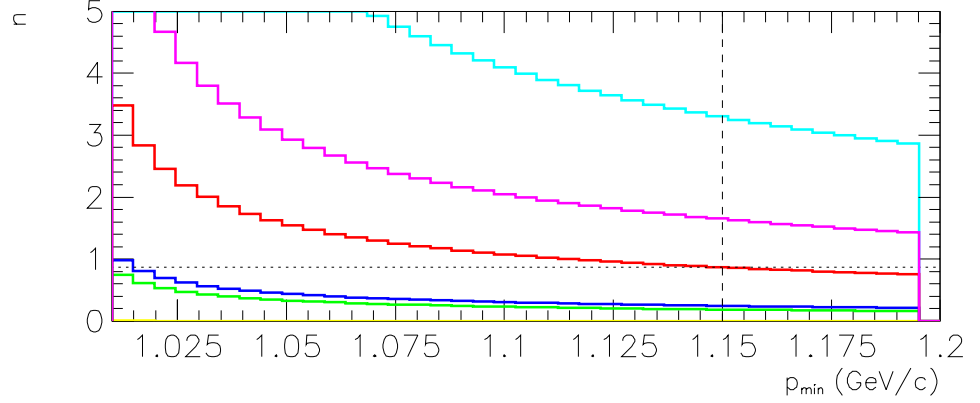


Figure 12: Assuming a refractive index n of a particle with a momentum p , a minimum momentum p_{min} is needed to produce Čerenkov light for a refractive index n , depending on the mass of the particle; this plot shows p_{min} vs. n , for e^\pm (bottom, yellow curve), μ^\pm , π^\pm , K^\pm , p/\bar{p} , and d (top, cyan curve).

π^\pm , K^\pm , p/\bar{p} , and d . To produce Čerenkov light at $n = 1.15$ the minimum momentum for kaons is $p_{min}=0.9$ GeV/c.

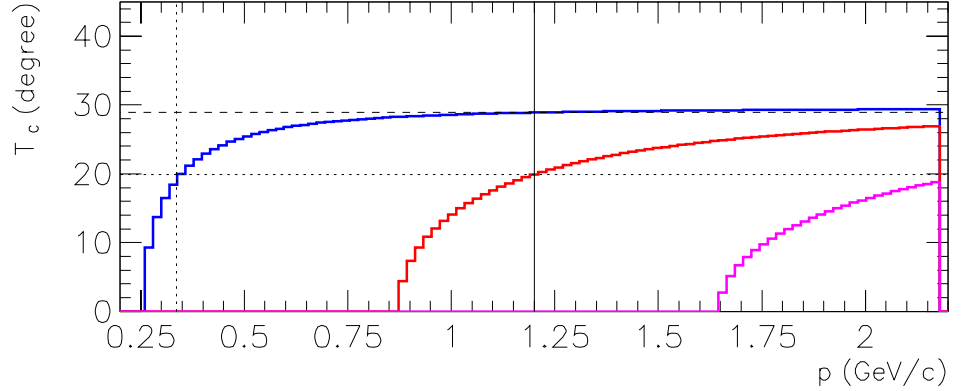


Figure 13: Čerenkov light emission angle Θ_C vs. particle momentum p (same as Fig. 11), but at fixed refractive index $n = 1.15$ and only for $\pi^\pm i$ (top, blue), $K^\pm i$ (middle, red), and p/\bar{p} (bottom, purple); the additional lines show the particle separation at constant momentum $p=1.2$ GeV/c.

At $n = 1.15$ and $p=1.2$ GeV/c the Čerenkov light emission angle Θ_C from kaons is $\Theta_C(K)=20^\circ$ and for pions it is $\Theta_C(\pi)=29^\circ$, as seen in Fig. 13. These angles correspond to a ring radius of 3.6 cm for kaons vs. 5.5 cm for pions at a distance of $d=10$ cm between KATC and KATP. The ring radius r will never be smaller than $r_{min}=d_{min} \times \tan \Theta_C$. KATC is a block of silica aerogel material. Its current design thickness is 4 cm. Thus the range of the ring radius for kaons is 3.6 cm to 5.1 cm, for pions it is 5.5 cm to 7.8 cm. These numbers can be tuned by decreasing the thickness of KATC. With a thickness of 2 cm one would get a range of the ring radius for kaons between 3.6 cm to 4.4 cm, and for pions between 5.5 cm to 6.7 cm. The close margins for a thickness of 4 cm does not raise a problem for the purity of the kaon identification, because with a simple upper cut on the ring radius one can eliminate any possible contamination by pions. The only loss would be in the kaon yield and, if KATZ is being part of a kaon trigger, than this would also imply a decreased event rate. But this does not work the same way if KATZ is being used for pion identification. At higher mass

there is no risk from any proton contamination of the kaon sample, because for a refractive index $n = 1.15$ the protons would have to have a minimum momentum $p_{\min} > 1.6$ GeV/c in order to emit any Čerenkov light, as shown before in Fig. 13. For pion detection one would have to reduce the thickness of KATC to e.g. 2 cm. But less Čerenkov material also means fewer Čerenkov photons. For $n = 1.15$ the ring image diameter from 1.2 GeV/c kaons will be the same as from 0.35 GeV/c pions. This illustrates the impressive capability of KATZ to separate kaons and pions. Another feature of KATZ is to perform a high precision 4-momentum measurement. All features combined KATZ demonstrates an unprecedented particle identification for CLAS.

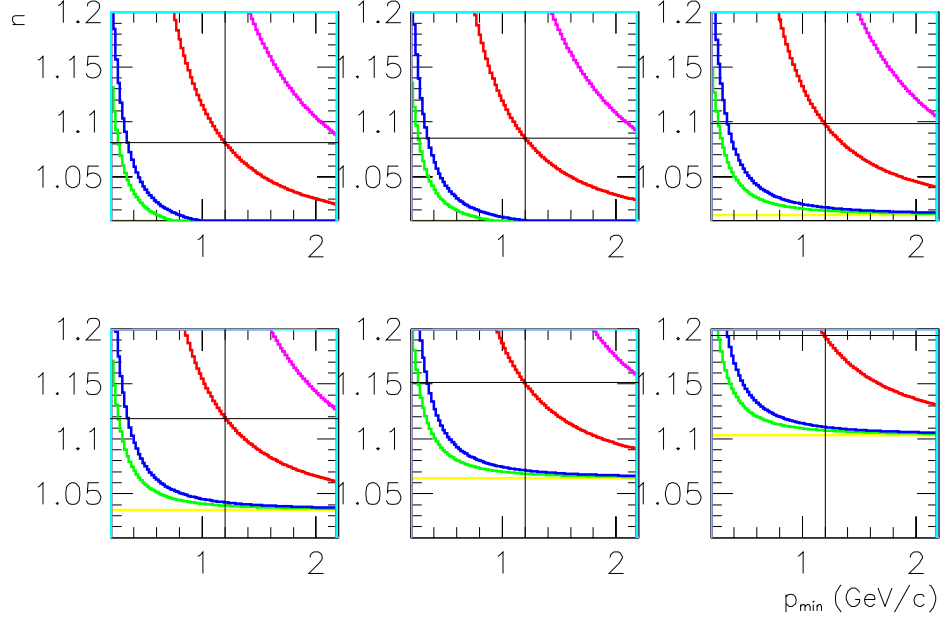


Figure 14: For a fixed Čerenkov light emission angle $\Theta_{\check{C}} = 1, 5, 10, 15, 20$, and 25° (top left to bottom right), these plots show the refractive index n vs. the particle momentum p ; each for e^\pm (bottom, yellow curve), μ^\pm , π^\pm , K^\pm , p/\bar{p} and d (top, cyan curve).

Another way to optimize the refractive index n is presented in Fig. 14. Here one starts with the required Čerenkov light emission angle $\Theta_{\check{C}}$ first, and then looks up the refractive index n as a function of the momentum p for any particles included in these plots.

An interesting option of KATZ is to utilize it for pion/muon separation by adjusting the refractive index to $n = 1.05$. Further GEANT simulations are needed to elaborate this interesting feature. With currently available Silica Aerogel from commercial sources there is no possibility to produce Čerenkov light from protons with a momentum below 1.5 GeV/c.

D.1.3 CaF₂ plane and multi-wire proportional chamber KATP

There are various options to detect the Čerenkov light. We suggest the use of a CaF₂ plane followed by a single plane multi-wire proportional chamber with plane of cathode pads (KATP). The hit position, and thereby the ring image, is measured through the charge induced on the cathode pads. This is the CLEO-III design[CLEO01]. Further details such as the importance of a sawtooth-shaped radiator should be studied later for the final design.

The CaF₂ plane's contribution to the detector efficiency and multiple scattering is automatically included in the simulation by the definition of its volume and material.

Another important criteria could be the point in time of the hits in KATP with respect to the trigger. By combining the hit location and the time one could reduce contribution from background,

in particular tracks coming from the beam halo. The best solution to determine the point in time of multiple tracks within the trigger time window would be with pipeline TDC's. To achieve good spacial resolution one would require a large number of wires and pads. But the number of hits from the track which we like to measure is fairly small and limited to a small area. A good compromise is to read out all pads through their individual discriminators and store all individual hits in the data stream of the event, but then multiplex pads through a logical or-function and use those combined signals as input for the pipe line TDC's. This technique, combined with the time information from the scintillators KATS and KATT and the track location from KATD and KATF helps to reduce the background. A detailed simulation will show how well this approach works.

The fast multi-wire proportional chamber KATP can also be used as input for a level 2 trigger, by matching the hit pattern with a lookup table. Events in a certain range of β can be selected with this level 2 trigger. In first order one could assume that the pattern does not depend on the location of the ring. This would simplify the lookup table.

D.2 Time-of-flight measurement with KATS and KATT

KATZ possibly includes two scintillator detectors, KATS and KATT, however it may be that KATS coupled with the timing scintillators in CLAS will be sufficient unless the particles are so far forward in angle that they do not reach the back scintillators. In this situation KATT would be used.

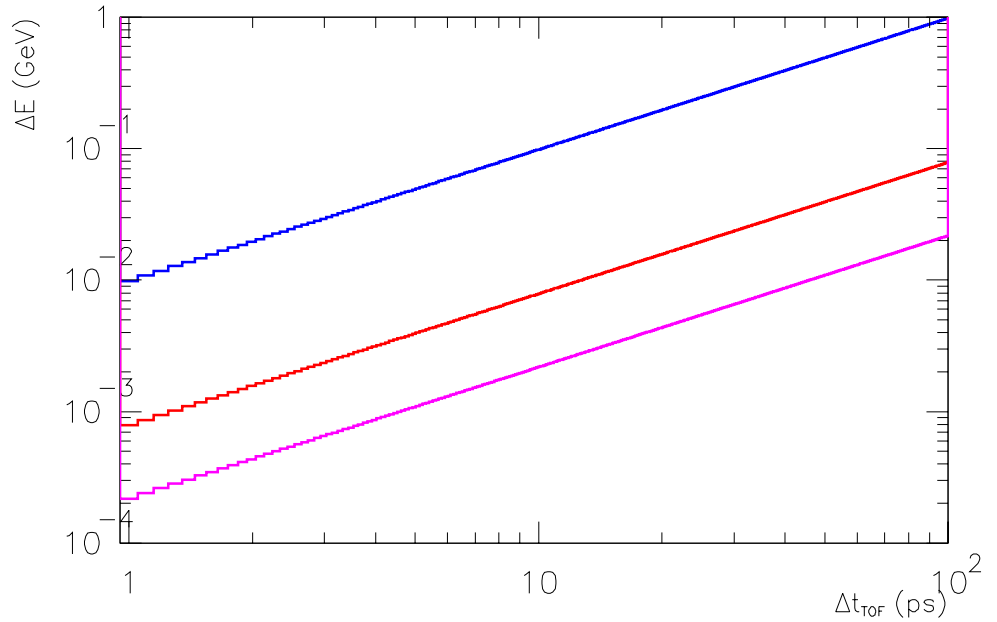


Figure 15: Energy resolution ΔE vs. time-of-flight resolution Δt_{TOF} at momentum $p = 1.2 \text{ GeV}/c$ for π^\pm (top, blue), K^\pm (middle, red), p/\bar{p} (bottom, violet)

Figure 15 shows for KATZ the energy resolution ΔE versus the time-of-flight resolution Δt_{TOF} between KATS and KATT at a momentum $p = 1.2 \text{ GeV}/c$ for π^\pm (top, blue), K^\pm (middle, red), p/\bar{p} (bottom, violet).

The signal from KATS can be used for the level 1 trigger. In addition the TOF measurement can be used to recalculate the point in time of the reaction at the vertex. This information in turn is used together with the RF signal from the accelerator to match the right electron bucket. Finding the right electron bucket is needed to find the right beam photon energy, either of the real or virtual photon.

Especially in electro-production we expect a considerable background rate from particles coming from the beam line. The number of accidental coincidences in KATS and KATT can be reduced

with tight time windows. However, if this cut is ineffective, then high resolution pipeline TDC's are needed. A more detailed study is needed. Experimental data needs to be compared with a simulation to decide if single-hit TDC's are going to be sufficient.

The scintillators of KATS and KATT are kept thin for optimum time resolution. Nevertheless, energy loss in these scintillators needs to be corrected for. The energy loss measurement is also independent of the time-of-flight measurement Therefore all scintillators

D.3 Drift chambers KATD and KATF

The tracking detector KATD can be either a silicon strip detector [?] or a drift chamber. The design KATF is a drift chamber based on the proven and tested concept of drift cells with regular polygon shape [MESTXX] [CLAS03]. Each drift cell forms a hexagon, with the sense wire at its center and potential wires at each of the six corners. Drift cells in one plane form a drift cell plane. Consecutive planes are staggered by one inner drift cell radius. Adjacent drift cells share two potential wires. A group of three planes form one layer. The direction of all drift wires within one layer is the same. Subsequent layers are separated by a plane of guard wires to separate the electrical field of two layers. The guard wires replace in position and orientation the sense wires of a fourth plane.

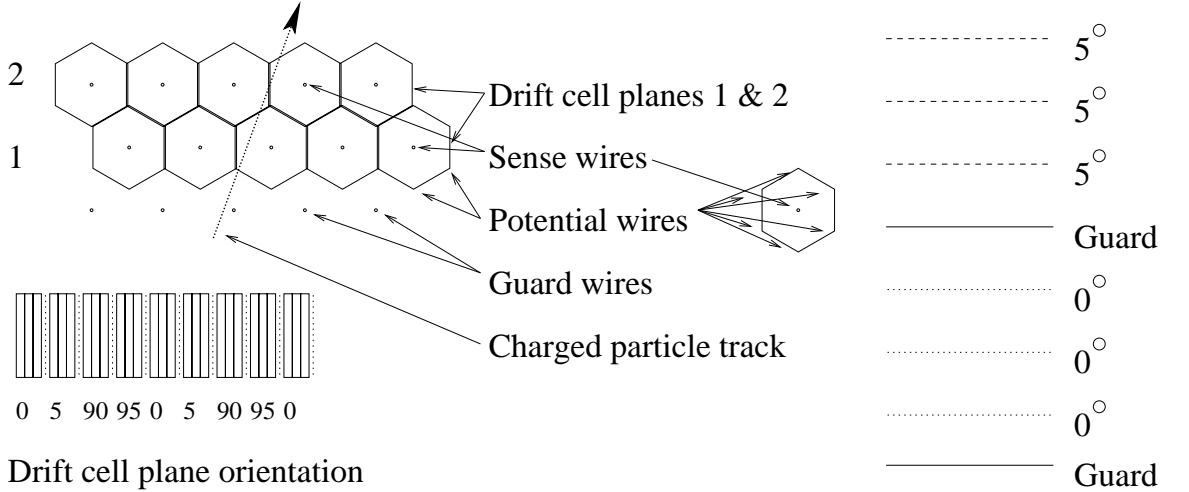


Figure 16: A view of the drift cells in the drift chambers (KATD and KATF); left top drawing illustrating 2 staggered planes of drift cells in one orientation, plus a plane of guard wires and a crossing charged particle track; center drawing showing a single drift cell; right drawing indicating one guard plane and one layer as sequence of three drift cell planes, followed by the next layer of different orientation; bottom right illustrating the sequence of multiple layers with all orientations listed (0° , 5° , 90° , and 95°).

Figure 16 illustrates the drift cells. The distance between a track of a charged particle and a cell's signal wire is measured as drift time. Naturally the drift cells are staggered, as shown in the top left panel of Fig. 16. Staggered drift cells help to resolve the left-right ambiguity of each drift cell's drift time measurement.

Adjacent cells share potential wires. This reduces the number of wires needed and arranges for an identical and symmetric electrical field in each drift cell. For a 3-dimensional tracking drift cells are needed with two orientations, preferably orthogonal with frequent alteration. But a change of the wire orientation causes a inhomogeneity of the electrical field. Therefore a plane with guard wires instead of signal wires is inserted between two planes of different orientation. Three planes with the same orientation form one layer. The layers are separated by the planes with guard wires. The guard wires not only help to form the electrical field between two planes of different orientation, but they also help to separate the ion and electron avalanches between different planes. An interference between two adjacent wires of the same orientation can be helpful to resolve the

left-right ambiguity. But an interference between two adjacent wires of different orientation would unnecessarily complicate the tracking algorithm. The sequence of signal and guard wires is also shown in the right panel of Fig. 16.

The bottom left panel of Fig. 16 illustrates the sequence of layers with different orientation. Stereo layers with an angle of 5° and 95° are inserted between 0° and 90° layers. The stereo layers are used by the tracking to combine the orthogonal hit coordinates from the 0° and 90° layers. They are also useful to resolve the left-right ambiguity. With this arrangement the drift chambers need only readout electronics attached to one end of each wire. The drift time is measured with one TDC channel per wire. Multiplexing is known to cause trouble for the drift chamber tracking algorithm. ADC's are not used.

A magnetic field between KATD and KATF is utilized to bend the tracks of charged particles. The direction and radius of each track's curvature is used to measure the particle's momentum. The design value of the spacial resolution is about $50 \mu\text{m}$. Only moderate momentum resolution is needed for particle identification by KATZ thanks to its RICH components. But excellent spacial resolution is of paramount importance for the momentum measurement when it is used to determine the energy of a particle.

The drift chamber KATF is used as lever arm to pinpoint the ring center in KATP. This fixes the center of the ring image, one very important point in the image seen by KATP. In fact only one additional hit from one photoelectron of the Čerenkov light cone would be needed to measure the Čerenkov light emission angle Θ_C . However, for practical reasons, such as background reduction, at least a second hit is required on the ring.

KATF is also used to determine the spacial interaction point of the charged particle with the TOF scintillator KATT. This is important to correct the measured time-of-flight.

As mentioned before, KATZ uses particle identification and momentum measurement to measure the particle energy. The energy of the kaon is used to tag on the formation of a ^4H in [HUNG04]. This tagging can also be done online as part of the level 1 trigger with a broad TOF cut, as discussed before in section D.2. But to achieve the required energy resolution an offline analysis of the drift chamber data is needed.

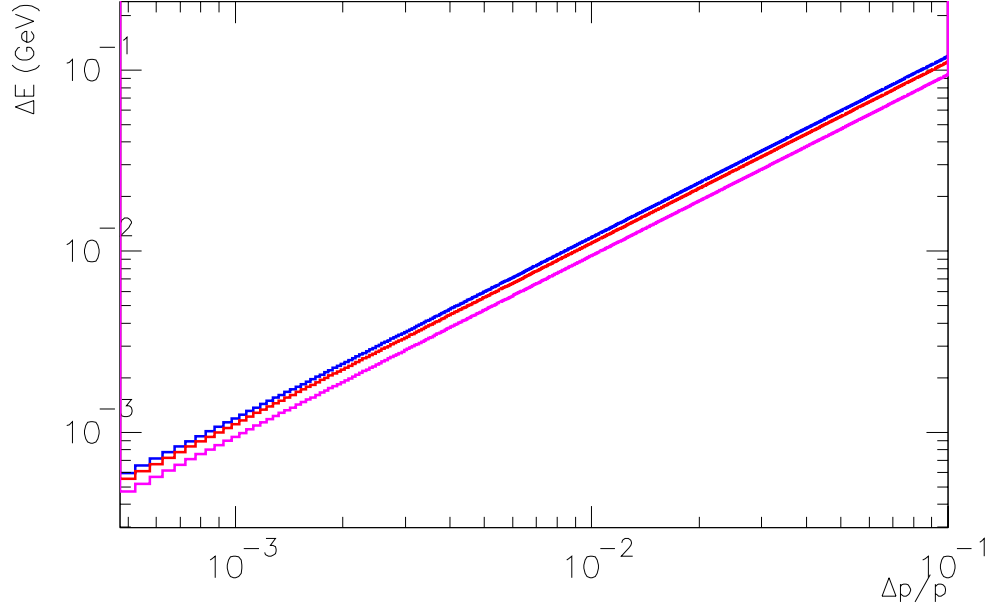


Figure 17: Energy resolution ΔE vs. relative momentum resolution $\frac{\Delta p}{p}$ at momentum $p = 1.2 \text{ GeV}/c$ for π^\pm (top, blue), K^\pm (middle, red), p/\bar{p} (bottom, violet)

Figure 17 shows the energy resolution ΔE versus the relative momentum resolution $\frac{\Delta p}{p}$ at a momen-

tum $p = 1.2$ GeV/c for π^\pm (top, blue), K^\pm (middle, red), p/\bar{p} (bottom, violet). An energy resolution can be achieved even at a moderate relative momentum resolution of about $\frac{\Delta p}{p} \leq 5 \times 10^{-3}$, or $\Delta p = 0.006$ GeV/c at $p=1.2$ GeV/c.

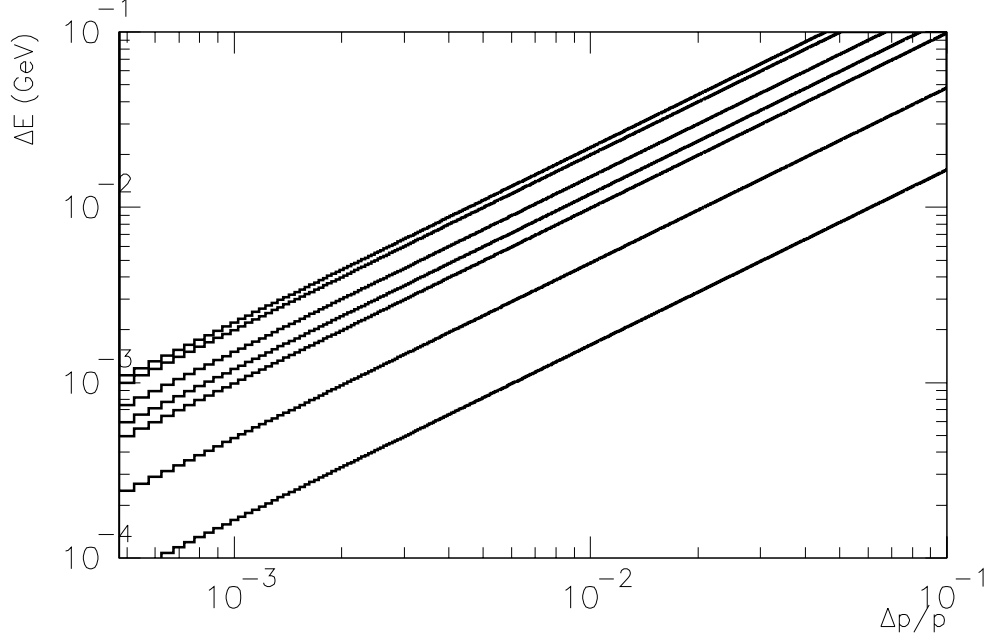


Figure 18: Energy resolution ΔE vs. relative momentum resolution $\frac{\Delta p}{p}$ for pions at momentum $p = 0.2$ (bottom), 0.5, 1.0, 1.2, 1.5, 1.5, 2.0, and 2.2 (top) GeV/c

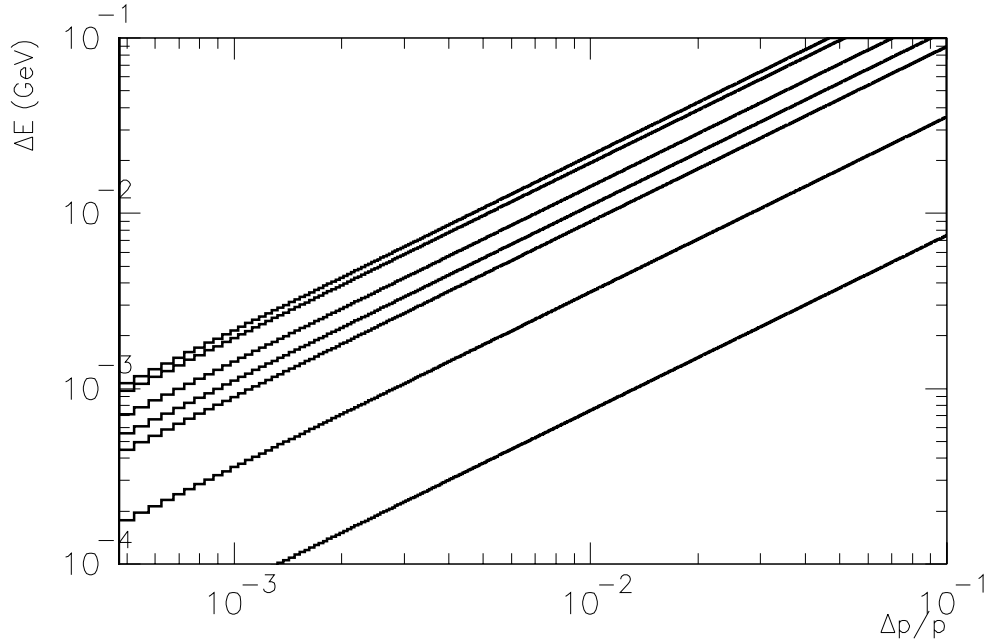


Figure 19: Energy resolution ΔE vs. relative momentum resolution $\frac{\Delta p}{p}$ for kaons at momentum $p = 0.2$ (bottom), 0.5, 1.0, 1.2, 1.5, 1.5, 2.0, and 2.2 (top) GeV/c

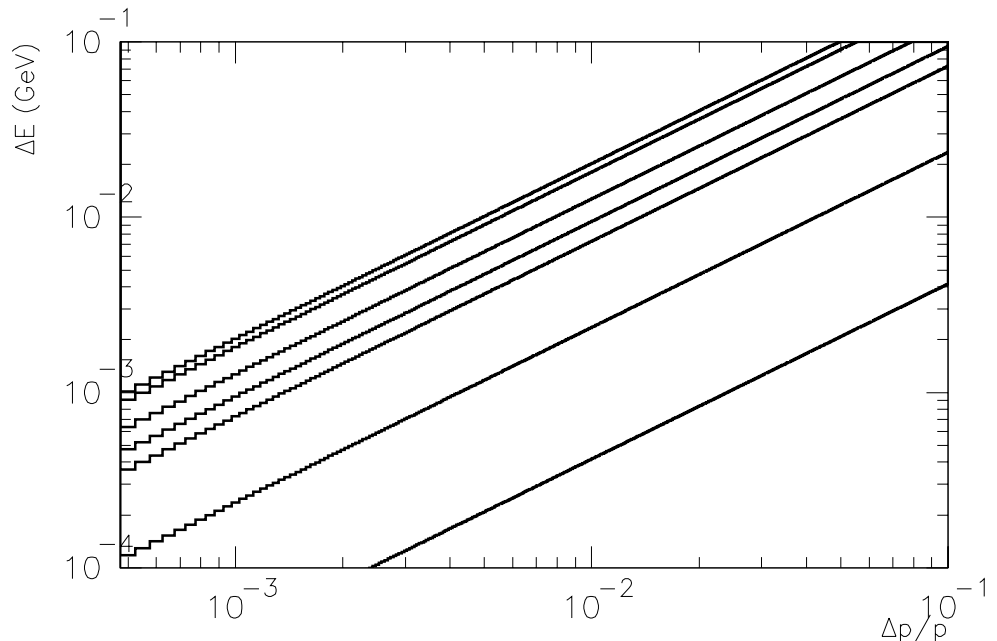


Figure 20: Energy resolution ΔE vs. relative momentum resolution $\frac{\Delta p}{p}$ for protons at momentum $p = 0.2$ (bottom), 0.5, 1.0, 1.2, 1.5, 2.0, and 2.2 (top) GeV/c

For some experiments it may be important to know the expected energy resolution ΔE versus the relative momentum resolution $\frac{\Delta p}{p}$ for pions, kaons, and protons, as a function of the particle momentum p . These numbers are plotted in Fig. 18, 19, and 20.

We can estimate the momentum resolution [BLUM94]. Assuming a track length $L=30\text{cm}$ through KATD, a point-measuring accuracy $\epsilon = 50 \mu\text{m}$, 30 wires with optimum wire spacing used for the momentum measurement, with a plane-to-plane distance of 0.4 cm, a magnetic field of about 1.5 T, approximately 90° angle between the magnetic field and a momentum $p=1.2 \text{ GeV/c}$, we get a relative momentum resolution $\frac{\delta p}{p} = 0.005$. With further optimization of the layout and the orientation of the wires in KATD we can further improve the resolution. In addition we intend to use the existing CLAS drift chambers as well. The momentum resolution is primarily limited by multiple scattering.

D.4 Triggers

The trigger of CLAS has two levels, 1 and 2. The trigger level 1 is the fastest trigger. Its purpose is to start the data taking process for one event as soon as a minimum condition was fulfilled. This may start the integration of ADC's or serve as common start or stop signal for TDC's. Experiments may run with trigger level 1 only. In this case the trigger would also initiate the readout of all data. The point in time of the trigger level 1 signal is well known. It can for instance be used for a time difference measurement with TDC's. After a readout all electronics, such as ADC's and TDC's, is reset for the next event. Data taking, readout and reset require considerable time and limit the event rate of the data acquisition system. In addition the maximum event rate may also be limited by the data acquisition system. In any case it may be desirable to reduce the event rate by reducing the rate of background events.

The purpose of trigger level 2 is to reduce the event rate from trigger level 1 by a more detailed analysis of each events. It is delayed, because it is formed from signals which require more processing time. Therefore the timing of trigger level 2 is normally not useful for time measurements. When combined, trigger level 1 and 2 will only initiate the readout of all data when both trigger level conditions are fulfilled. Otherwise, if trigger level 1 condition is fulfilled, but trigger level 2 condition is not, then the data taking process will be interrupted and all electronics is fast reset. For ADC's

and TDC's the fast reset may be significantly faster than the regular reset after a completed data taking cycle.

After a completed readout the data acquisition system also has to distribute the data for data storage. The performance can be improved by an asynchronous distribution. This would be typically implemented with a queueing solution. This way one would better utilize the varying time between events. However, the gain would be still limited to the average event rate. If the data storage component of the data acquisition system is limiting the experiment's event rate, then a trigger level 3 could be used to perform a further data reduction by removing more background events before the data are distributed for data storage. *I need to verify if this option is already in use, but AFAIK it is not.*

In a typical photoproduction run the trigger level 1 requires a signal from the tagging system, one start scintillator (ST) and a time-of-flight scintillator (SC) in coincidence. ST is not used for runs with KATZ. In addition SC may not be needed or even wanted as trigger component either. KATS replaces ST for trigger level 1. In addition a coincide between a signal from KATS and KATT are required for trigger level 1. Geometrical matching between KATS and KATT are also included in the trigger level 1 condition. Tight cuts on the time-of-flight between KATS and KATT can be used to select, for example, kaons within a specific energy range. Of course at this point there is no particle identification done yet and therefore the kaon sample would be highly contaminated by pions and protons. A pulse height cut can be used to include energy loss in trigger level 1, thereby optimizing the kaon-to-pion ratio of trigger level 1.

Trigger level 2 is implemented based on hit patterns from KATD, KATF and KATP. A rough momentum measurement with KATD is performed by lookup tables. The curvature of a track fragment is translated into a momentum. A simple correlation between a spacial point downstream in KATF and all points in KATP is used to select the center of a ring image in KATP. The radius of the ring image radius is then determined by matching a hit pattern in KATP with another lookup table. The combination of the curvature and radius form trigger level 2. Some of these criteria, in particular the ring image radius, could be also implemented with fast electronics for trigger level 1. It is important to reduce the pion background from the kaon signal as fast early as possible from the trigger.

A multiplicity cut in the drift chambers KATD and KATF could be used as additional criteria for trigger level 2. The charge of the particle could be another criteria. For example, if the experiment only requires K^+ in KATZ, then a cut on the charge would remove the large background from π^- . Even a simple tracking could be performed by hardware with simple firmware using the Principal Components Analysis (PCA) as trigger level 3 for a better kaon-to-pion ratio.

D.5 Alternatives

Various KATZ components could be implemented using a different techniques. The following paragraphs list such alternatives and discusses the pro and cons.

D.5.1 Čerenkov detectors

There are two ways to design a Čerenkov detector. Either one utilizes the threshold effect and uses the detector only to veto on certain particles or, and this is what is presented in the final design, one actually measures the angle of the emitted Čerenkov light.

For the purpose of pion-kaon separation with a threshold counter one would adjust the refractive index so that pions emit Čerenkov light, while kaons at the same momentum do not. It should be noted that neither will protons with the same momentum produce Čerenkov light. The signal from the Čerenkov detector would be used to veto pions. The advantage of this concept is that the particle identification can be easily integrated into the trigger. The contamination of the kaons with pions depends on the detector's pion detection efficiency. This concept works fine for experiments where the particle momentum is limited to a small range, for example in a beam line for mesons. A

Čerenkov detector for [HUNG04] might work. But the entire KATZ detector is fairly complex and turns out to be an asset for new physics with CLAS. Therefore the refractive index is adjusted so that kaons produce Čerenkov light, too. The separation of kaons and pions is done by comparing the Čerenkov light emission angle Θ_C and the particle's momentum. Time-of-flight and energy loss are used as additional criteria.

There are various ways to measure the Čerenkov light emission angle Θ_C , for example the photon detector described by the RICH detector described above.

E Software

The analysis of the data from KATZ requires a fair amount of software. The software can be grouped into three classes. The first one is the simulation. GEANT is the primary tool used for the simulation. The second class is the data evaluation code to process experimental data². The data evaluation code also has to be able to process simulated data. The third class is the physics analysis code. Its purpose is to cooperate with other existing physics analysis code and help to extract the necessary physics related information. The following sections describe all three classes, as far as they already exist.

E.1 GEANT simulation

The existing GEANT simulation of KATZ already includes all detectors, their volumes and all active materials. The material of the support structure has not been added yet.

Particles can interact with the detectors' material and thereby produce *hits*. The hits are used by the simulation to emulate a detector response, which then are stored as digitizations. The hits and digitizations include the volume names, volume numbers if multiple replica of the same volume form a detector, and of course the simulated physical data like the location, energy loss etc. for hits and simulated experimental data like ADC and TDC values for the digitizations.

The digitizations are calculated under ideal conditions by the GEANT simulation. A second tool is used to read in the simulated data from a GEANT data file, add proper errors to the digitizations and then write the result into a new GEANT data file. This two-step process allows us to study the effect of the detectors' limited resolution with the same ideal data set under varying conditions. It also saves a lot of computing time. The GEANT simulation itself requires a great amount of computing time. The additional step of adding simulated errors to the digitizations requires only a minimum of computing time.

The GEANT simulation already accounts for effects like multiple scattering, energy loss, radiation losses and particle decay. All these features can also be disabled in the simulation. The total contribution from the physical effects plus the limited resolution of the detectors can be very difficult to calculate in an empiric formula. The multi-step simulation simplifies this matter a great deal.

The GEANT simulation of KATZ requires several features which are often disabled in typical CLAS simulations. For example Čerenkov light production has to be enabled with the CKOV option. Rayleigh scattering of photons has to be enabled. The cut-off energy of photons, leptons and hadron has to be lowered within some KATZ volumes, and possibly also in other regions of CLAS if the particles can reach KATZ from there.

Various KATZ components need to be studied with the simulation under different aspects.

Čerenkov light emission in KATC is simulated by GEANT. So is the photon yield, conversion on the CaF₂ plane and of course the electron tracking through KATP. This detailed simulation shows a more accurate picture of the detector performance than a simplified calculation based on an empirical formula for the efficiency.

²In CLAS terms this would be called "cooking".

List of Figures

1	Experimental Spectrum of proton emission from the non-mesonic weak decay of ${}^4_{\Lambda}\text{He}$. The Curve is only to guide the eye	5
2	Experimental Spectrum of neutron emission from the non-mesonic weak decay of ${}^5_{\Lambda}\text{He}$. The Histogram is the theoretical calculation	7
3	The Level Diagrams for S-shell Hypernuclei	8
4	Experimental Layout for the Hypernuclear Experiment in HallC. The same electron tagging system would be used while the kaons would be detected in CLAS for the ${}^4_{\Lambda}\text{H}$ measurement	12
5	The Virtual Flux Factor for 1800 MeV Electrons as a Function of Polar Angle for Approximately 1500 MeV Photons	13
6	The Virtual Flux Factor Integrated for a 1800 MeV Electrons Integrated over the Electron Solid Angle as a Function of Polar Angle for 1500 MeV Photons	14
7	K ^A TZ at work [UNKNWN].	17
8	A schematic of KATZ, left panel showing a topview of all six KATZ components (KATS, KATD, KATC, KATF, KATP and KATT) for one CLAS sector, right panel show a cross section of KATZ.	19
9	A new target cylinder to operate KATZ.	20
10	Čerenkov light emission from interaction of a charged particle with a radiator and the projection of the Čerenkov light as ring image onto a photon detector.	21
11	Čerenkov light emission angle $\Theta_{\check{C}}$ vs. particle momentum p , with refractive index $n = 1.05$ (top left), $n = 1.10$ (top right), $n = 1.15$ (bottom left), and $n = 1.20$ (bottom right); each for e^{\pm} (top, yellow curve), μ^{\pm} , π^{\pm} , K^{\pm} , p/\bar{p} , and d (bottom, cyan curve, <i>not seen</i>).	23
12	Assuming a refractive index n of a particle with a momentum p , a minimum momentum p_{\min} is needed to produce Čerenkov light for a refractive index n , depending on the mass of the particle; this plot shows p_{\min} vs. n , for e^{\pm} (bottom, yellow curve), μ^{\pm} , π^{\pm} , K^{\pm} , p/\bar{p} , and d (top, cyan curve).	24
13	Čerenkov light emission angle $\Theta_{\check{C}}$ vs. particle momentum p (same as Fig. 11), but at fixed refractive index $n = 1.15$ and only for π^{\pm} (top, blue), K^{\pm} (middle, red), and p/\bar{p} (bottom, purple); the additional lines show the particle separation at constant momentum $p=1.2$ GeV/c.	24
14	For a fixed Čerenkov light emission angle $\Theta_{\check{C}} = 1, 5, 10, 15, 20$, and 25° (top left to bottom right), these plots show the refractive index n vs. the particle momentum p ; each for e^{\pm} (bottom, yellow curve), μ^{\pm} , π^{\pm} , K^{\pm} , p/\bar{p} and d (top, cyan curve).	25
15	Energy resolution ΔE vs. time-of-flight resolution Δt_{TOF} at momentum $p = 1.2$ GeV/c for π^{\pm} (top, blue), K^{\pm} (middle, red), p/\bar{p} (bottom, violet)	26
16	A view of the drift cells in the drift chambers (KATD and KATF); left top drawing illustrating 2 staggered planes of drift cells in one orientation, plus a plane of guard wires and a crossing charged particle track; center drawing showing a single drift cell; right drawing indicating one guard plane and one layer as sequence of three drift cell planes, followed by the next layer of different orientation; bottom right illustrating the sequence of multiple layers with all orientations listed (0° , 5° , 90° , and 95°).	27
17	Energy resolution ΔE vs. relative momentum resolution $\frac{\Delta p}{p}$ at momentum $p = 1.2$ GeV/c for π^{\pm} (top, blue), K^{\pm} (middle, red), p/\bar{p} (bottom, violet)	28
18	Energy resolution ΔE vs. relative momentum resolution $\frac{\Delta p}{p}$ for pions at momentum $p = 0.2$ (bottom), 0.5, 1.0, 1.2, 1.5, 1.5, 2.0, and 2.2 (top) GeV/c	29
19	Energy resolution ΔE vs. relative momentum resolution $\frac{\Delta p}{p}$ for kaons at momentum $p = 0.2$ (bottom), 0.5, 1.0, 1.2, 1.5, 1.5, 2.0, and 2.2 (top) GeV/c	29
20	Energy resolution ΔE vs. relative momentum resolution $\frac{\Delta p}{p}$ for protons at momentum $p = 0.2$ (bottom), 0.5, 1.0, 1.2, 1.5, 1.5, 2.0, and 2.2 (top) GeV/c	30

List of Tables

1	Allowed Transitions in $(2I+1)(2S+1)L_J$ Notation	4
2	Comparison of Calculated Values of the Asymmetry Parameter, a_Λ to Experiment .	6
3	Experimental Parameters of S-shell Hypernuclear Decay in Terms of the Λ Free Decay Width [†]	10
4	Expected counts for decay of $^4_\Lambda\text{H}$	15
5	Relative position (cm) of each KATZ component in Z-direction (along the beam line).	20

References

- [1] Particle Data Group, Phys. Rev. **D54** (1996) 50.
- [2] E.D. Commins and P.H. Bucksbaum, *Weak Interactions of Leptons and Quarks*, Cambridge Univ. Press, UK (1983).
- [3] F.J. Gilman and M.B. Wise, Phys. Rev. **D20**, (1979) 2392.
- [4] L. Okun, *Leptons and Quarks*, North Holland, The Netherlands (1982). $\Gamma_{\Lambda}/\Gamma_{free} = 1.36$;
- [5] N. Isgur, *et al*, Phys. Rev. Lett. **64** (1990) 161.
- [6] K. P. Gall, PhD Dissertation, Boston University, 1989, unpublished.
- [7] T. Motoba, Nucl. Phys. **A547** (1992) 115c, and references therein.
- [8] B. F. Gibson and E. V. Hungerford, Physics Reports, **257**(1995)349
- [9] T. Inoue, S. Takeuchi, and M. Oka, Nucl. Phys. **A597** (1996) 563.
- [10] K. Maltman and M. Shmatikov, Nucl. Phys. **A585** (1995) 343c.
- [11] G. Keyes, *et al*, Nuo. Cim. **31A** (1976) 401.
- [12] J. J. Szymanski, *et al*, Phys Rev **C43** (1991) 849.
- [13] R.H. Dalitz and L. Liu, Phys. Rev. **116** (1959) 1312.
- [14] R.H. Dalitz and G. Rajasekharan, Phys. Lett. **1** (1962) 58.
- [15] M.M. Block and R.H. Dalitz, Phys. Rev. Lett **11** (1963) 96.
- [16] J. Cohen, Progress in Particle and Nuclear Physics **25** (1990) 139.
- [17] C. Bennhold, *et al*, Phys. Rev. **C45** (1992) 947.
- [18] G. Garbarino, A. Parreno, and A. Ramos, Preprint arXiv:nucl-th/0212084v2, Jan 17, 2003.
- [19] J.F. Duach, G.B. Feldman, B.R. Holstein, Ann. Phys. **249**(1996)146.
- [20] W. M. Alberico and G. Garbarino, Physics Reports, **369**(2002)1-109.
- [21] C.B. Dover, Few-Body Systems, Suppl. **2** (1987) 77, J. Cohen, Phys. Rev. **C42** (1990) 2724, R.A. Schumacher, Nucl. Phys. **A547** (1992) 143c, N. Lee, H. Jong, and D. Cha, nucl-th/9608006, xxx.lanl.gov e-Print archive (1996).
- [22] M.M. Block, *et al*, Nuovo Cim. **28** (1962) 299.
- [23] A. Ramos, E. Oset, and L.L. Salcedo, Nucl. Phys. **A585** (1995) 129c.
- [24] R.A. Schumacher, in *Properties & Interactions of Hyperons*, Ed. B.F. Gibson, P.D. Barnes, K. Nakai, World Scientific, Singapore (1994) 85.
- [25] V.J. Zeps and G.B. Franklin, Proc. INS Symposiom #23, Ed. S. Sugimoto and O. Hashimoto, Universal Academy Press, Tokyo (1995) 227.
- [26] H. Ota, *et al*, Nucl. Phys. **A585** (1995) 109c.
- [27] M. Athanas, Ph. D. thesis, Carnegie Mellon Univ. (1992) unpublished.
- [28] P.A. Katz, *et al*, Phys. Rev. **D1** (1970) 1267.
- [29] H. Tamura, *et al*, Phys. Rev. **C40** (1989) R479.
- [AERO98] <http://rd11.web.cern.ch/RD11/rkb/PH14pp/node4.html>
- [BLUM94] W. Blum, L. Rolandi, Particle Detection with Drift Chambers, ISBN 3-540-58322-X (1994).
- [CLAS03] B. Mecking *et al.*, Nucl. Instr. Meth. A **503**, 513 (2003).
- [CLEO01] The CLEO III Detector, <http://www.lns.cornell.edu/public/CLEO/spoke/CLEOc/pd2/partiv/partiv.ps> (2001).

- [GEANT3] R. Brun *et al.*, CERN Program Library Long Writeup, *GEANT - Detector Description and Simulation Tool*, W5013 (1994).
- [HUNG04] E. Hungerford, H. Juengst *et al.*, JLab PAC 26, *A Study of the Weak Decay of the S-Shell Hypernucleus, ${}^4_{\Lambda}H$ and the $\Delta I = 1/2$ Rule*, (2004).
- [JUEN01] H. Juengst *et al.*, in INPC2001, Berkeley 2001, Nucl. Phys. in the 21st Century (2001), p. 357.
- [MESTXX] M. Mestayer *et al.*, Nucl. Instr. Meth. ???.
- [NASA99] NASA, Mars Climate Orbiter Mishap Investigation Board, Report (1999).
- [PDG02] K. Hagiwara *et al.*, *Review of Particle Physics*, Phys. Rev. D **66**, 010001 (2002) [<http://pdg.lbl.gov/>].
- [SCHU04] J.W.C. McNabb, R.A. Schumacher, et al., Hyperon photoproduction in the nucleon resonance region, Phys. Rev. C, accepted for publication, (2004)
- [UNKNWN] Kudos to the unknown photographer.